J. Fluid Mech. (2023), *vol*. 972, A28, doi:10.1017/jfm.2023.708

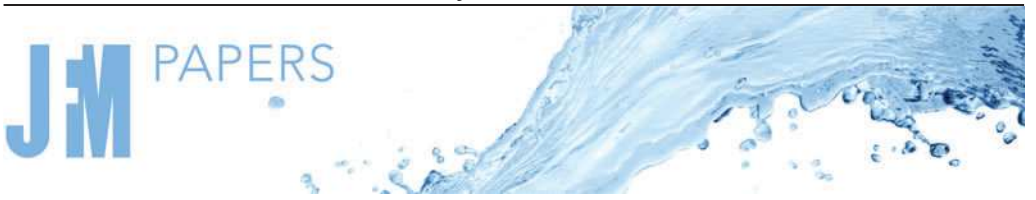

Detailed numerical investigation of the drop aerobreakup in the bag breakup regime

Y. Ling[1,2,†] **and T. Mahmood**[2]

[1]Department of Mechanical Engineering, University of South Carolina, Columbia, SC 29208, USA

[2]Department of Mechanical Engineering, Baylor University, Waco, TX 76798, USA

(Received 24 January 2023; revised 6 July 2023; accepted 22 August 2023)

Aerobreakup of drops is a fundamental two-phase flow problem that is essential to many spray applications. A parametric numerical study was performed by varying the gas stream velocity, focusing on the regime of moderate Weber numbers, in which the drop deforms to a forward bag. When the bag is unstable, it inflates and disintegrates into small droplets. Detailed numerical simulations were conducted using the volume-of-fluid method on an adaptive octree mesh to investigate the aerobreakup dynamics. Grid-refinement studies show that converged three-dimensional simulation results for drop deformation and bag formation are achieved by the refinement level equivalent to 512 cells across the initial drop diameter. To resolve the thin liquid sheet when the bag inflates, the mesh is refined further to 2048 cells across the initial drop diameter. The simulation results for the drop length and radius were validated against previous experiments, and good agreement was achieved. The high-resolution results of drop morphological evolution were used to identify the different phases in the aerobreakup process, and to characterize the distinct flow features and dominant mechanisms in each phase. In the early time, the drop deformation and velocity are independent of the Weber number, and a new internal-flow deformation model, which respects this asymptotic limit, has been developed. The pressure and velocity fields around the drop were shown to better understand the internal flow and interfacial instability that dictate the drop deformation. Finally, the impact of drop deformation on the drop dynamics was discussed.

Key words: drops, aerosols/atomization, multiphase flow

1. Introduction

When a drop is subjected to a high-speed gas stream, the drop can experience significant deformation or even breakup. If the stabilizing forces, including surface tension and viscous forces, are not sufficient to overcome the destabilizing inertia force, then the

† Email address for correspondence: stanley_ling@sc.edu

drop will break into a collection of child droplets of different sizes (Taylor 1949; Guildenbecher, López-Rivera & Sojka 2009; Theofanous 2011). The aerodynamic breakup (or aerobreakup) of drops is essential to many spray applications, such as liquid fuel injection and spray cooling, and has therefore been studied extensively in the past decades.

Though the interaction between the drop and surrounding gas in practical aerobreakup applications usually involves many complex factors, drop aerobreakup is formulated typically in a simplified configuration, i.e. an initially stationary and spherical drop is suddenly exposed to an unbounded uniform gas stream (Theofanous & Li 2008; Jain *et al.* 2019; Marcotte & Zaleski 2019). Then the two-phase interfacial flows that dictate the drop deformation and dynamics are fully determined by the densities and viscosities of the drop liquid and the gas, ρ_l, μ_l, ρ_g and μ_g, the surface tension σ, the initial drop diameter d_0, and the gas stream velocity U_0. The subscripts g and l are used to denote the properties for the gas and liquid, respectively, while the subscript 0 is used to represent the initial state. The drop is considered to be far away from the free-stream boundary. Furthermore, it is assumed that the Mach number of the gas stream is significantly lower than the critical Mach number, so the compressibility effect can be neglected. Aerobreakup of drops in a supersonic gas stream (Theofanous, Li & Dinh 2004; Theofanous *et al.* 2007; Sharma *et al.* 2021) is outside the scope of the present study. We have also considered the liquid as a Newtonian fluid and excluded the non-Newtonian effect of the drop liquids on the process (Joseph, Belanger & Beavers 1999; Theofanous, Mitkin & Ng 2013). As a result, the present problem can be characterized fully by four independent dimensionless parameters: the Weber number $We = \rho_g U_0^2 d_0/\sigma$, the Reynolds number $Re = \rho_g U_0 d_0/\mu_g$, the Ohnesorge number $Oh = \mu_l/\sqrt{\rho_l d_0 \sigma}$, and the gas-to-liquid density ratio $r = \rho_g/\rho_l$ (Pilch & Erdman 1987; Hsiang & Faeth 1992; Joseph *et al.* 1999; Guildenbecher *et al.* 2009). Alternative dimensionless parameters can be defined based on the above four parameters, such as the gas-to-liquid viscosity ratio $m = \mu_g/\mu_l$ (Guildenbecher *et al.* 2009).

The present study focuses on the regime of millimetre water drops in an air stream, following the recent work by Jackiw & Ashgriz (2021). In this regime, the small values of $r \sim O(10^{-3})$ and $Oh \sim O(10^{-3})$, and the large value of $Re \sim O(10^3)$, indicate that surface tension plays the dominant role in resisting drop breakup. The key parameter characterizing drop dynamics and morphology evolution is $We \sim O(10^2)$, which is moderate. Previous experiments using shock tubes (Hinze 1955; Hsiang & Faeth 1995; Joseph *et al.* 1999; Theofanous *et al.* 2004) and continuous jets (Liu & Reitz 1993; Flock *et al.* 2012; Zhao *et al.* 2013; Opfer *et al.* 2014; Guildenbecher *et al.* 2017; Jackiw & Ashgriz 2021, 2022) have identified different breakup modes for low-Oh drops. The critical Weber number for breakup to occur is $We_{cr} \approx 11 \pm 2$. When $We < We_{cr}$, the drop will oscillate without breakup or break into a small number of large child drops due to large-amplitude nonlinear oscillations (also referred to as the vibration breakup mode). As $We > We_{cr}$, the drop will break into a large number of child droplets. The drop morphology upon breakup varies significantly with We, from bag, bag-stem (or multi-mode), multi-bag and stripping (or sheet-thinning mode) (Hsiang & Faeth 1995; Liu & Reitz 1997; Guildenbecher *et al.* 2009; Jackiw & Ashgriz 2021). When We is sufficiently large, such as $We > 10^3$, it has been claimed in previous studies that the drop breaks in the catastrophic mode (Joseph *et al.* 1999). However, more recent high-resolution experimental diagnostics suggest that such a breakup mode does not exist (Theofanous & Li 2008). Different classifications of the breakup regimes have also been proposed, based on the dominant breakup mechanisms (Theofanous *et al.* 2004). Since the bag, bag-stem and multi-bag breakup modes all involve the formation and inflation of bags,

which is driven by the Rayleigh–Taylor instability, they have been reclassified as the Rayleigh–Taylor piercing mode. On the other hand, the sheet-thinning mode has been renamed the shear-induced entrainment mode, since it is driven mainly by the shear on the interface periphery.

The impulsive gas acceleration and continuous non-zero relative velocity between the gas and the drop induce both viscous and inviscid, steady and unsteady drag forces on the drop (Maxey & Riley 1983; Mei, Lawrence & Adrian 1991; Ling, Parmar & Balachandar 2013), resulting in a streamwise acceleration of the drop. As the drop deforms, the gas flow will be modulated, which in turn influences the drop deformation. Consequently, although the surrounding gas flow in the far field is steady, the drop deformation and the gas flow around the drop are highly unsteady. According to the scaling analysis (Ling *et al.* 2013), the ratios between the unsteady forces and the quasi-steady drag are proportional to $1/r$. For the present cases with $r \ll 1$, the unsteady forces will have a small contribution to the overall drop acceleration. The drop dynamics are dictated by the quasi-steady drag, and the drop velocity will increase following the gas viscous time scale. For cases with a large r, such as in a pressurized gas environment, the contribution of the unsteady forces to the drop acceleration cannot be ignored (Jain *et al.* 2019; Marcotte & Zaleski 2019).

Aerodynamic breakup of an isolated drop involves rich physics, and the investigation of the subject is challenging for both experiments and simulations. Due to the highly unsteady flow and complex topology change, an analytical approach is generally not viable, except for limiting cases (Vanden-Broeck & Keller 1980; Miksis, Vanden-Broeck & Keller 1981). Previous studies of drop aerobreakup are based on experiments. Thanks to advancements in high-speed imaging, the temporal evolution of the drop morphology can be captured clearly (Theofanous & Li 2008; Flock *et al.* 2012; Opfer *et al.* 2014; Jackiw & Ashgriz 2021). With more sophisticated diagnostics, such as digital in-line holography, the velocity and size of the child droplets can also be measured (Gao *et al.* 2013; Guildenbecher *et al.* 2017). However, it is still challenging to measure high-level details of the drop deformation and gas flows due to the small length and time scales involved. For example, for the bag breakup mode, it is difficult to visualize the velocity and pressure fields inside the bag and to measure directly the thickness and velocity in the bag sheet (Opfer *et al.* 2014). Therefore, high-fidelity interface-resolved numerical simulations that can provide these high-level details are essential to investigate drop aerobreakup (Jain *et al.* 2019; Marcotte & Zaleski 2019).

Fully-resolved simulations of drop aerobreakup are expensive if one aims to resolve all the length scales. For example, for a millimetre-sized drop that breaks in the bag mode, the bag sheet thickness reduces to tens of nanometres before the bag sheet ruptures (Williams & Davis 1982; Burelbach, Bankoff & Davis 1988). Previous numerical studies could afford to use a high mesh resolution for two-dimensional (2-D) axisymmetric simulations only (Han & Tryggvason 1999, 2001; Jing & Xu 2010; Chang, Deng & Theofanous 2013; Jalaal & Mehravaran 2014; Strotos *et al.* 2016; Stefanitsis *et al.* 2017; Jain *et al.* 2019; Marcotte & Zaleski 2019). However, as will be shown later, 2-D axisymmetric simulations will not correctly capture the bag formation in the high *Re* regime since the turbulent wake and its influence on the drop deformation are not resolved faithfully. That explains why even converged 2-D simulations fail to reproduce the bag morphology observed in experiments (Marcotte & Zaleski 2019). The mesh resolutions in previous three-dimensional (3-D) simulations are generally much lower, and are insufficient to capture the turbulent wake and the bag development (Kekesi, Amberg & Wittberg 2014; Jain *et al.* 2015, 2019; Yang *et al.* 2016). There remains a significant gap between the existing simulation results and experimental data.

An important motivation for the study of drop aerobreakup is to develop sub-scale models that can be used in simulations of sprays consisting of a huge number of droplets, for which it is intractable to resolve the interface of each individual drop. The cell size used for simulations of sprays in practical scales is typically much larger than the size of individual drops, therefore the drops are represented by Lagrangian point-particles (Apte, Gorokhovski & Moin 2003; Pai & Subramaniam 2006; Balachandar 2009). The drop motion, shape deformation, topology change, and heat and mass transfer between the drop and the surrounding flow need to be captured by subgrid models (O'Rourke & Amsden 1987; Hsiang & Faeth 1992). When drop breakup occurs, one also needs to estimate the starting time and end time (Chou & Faeth 1998; Dai & Faeth 2001) and the statistics of the child droplets produced (O'Rourke & Amsden 1987; Hsiang & Faeth 1992; Wert 1995; Zhao *et al.* 2013). For the moderate *We* regime, the Taylor analogy breakup (TAB) model (O'Rourke & Amsden 1987) and its subsequent variants (Tanner 1997; Park, Yoon & Hwang 2002) have been adopted widely to predict the drop deformation (the time evolution of the drop lateral radius) and the breakup time. The TAB models are based simply on the mass–spring–damper analogy, and there exist coefficients that need to be calibrated based on experimental data. Models that incorporate the flow physics have also been proposed. In the model of Villermaux & Bossa (2009), the pressure distribution induced by the stagnation flow on the windward surface is considered as the driving force for the lateral expansion of a thin liquid disk, although the model was also extended to predict the overall drop deformation (Kulkarni & Sojka 2014; Stefanitsis *et al.* 2019*b*; Rimbert *et al.* 2020; Jackiw & Ashgriz 2021). Since the Rayleigh–Taylor instability (RTI) plays a significant role in the formation and development of bags, models based on linear RTI analysis have also been developed to predict the critical condition for the bag formation and also the number of bags to be formed in the multi-bag mode (Harper, Grube & Chang 1972; Joseph *et al.* 1999; Theofanous *et al.* 2004). For very high *We*, the drop breaks in the stripping mode, and the corresponding breakup models are based on the shear instability (Ranger & Nicholls 1969) and the rupture of the thinning liquid sheets (Liu & Reitz 1997; Lee & Reitz 2001). Comprehensive reviews of these models have been given in previous studies (Guildenbecher *et al.* 2009; Jackiw & Ashgriz 2021), thus are not repeated here.

Though significant progress has been made in understanding the physics that drives the deformation and breakup of drops at moderate *We*, important fundamental questions remain unanswered. When *We* is just above the critical value, a single bag is formed, and the breakup starts when the bag sheet ruptures. When *We* is very large, liquid sheets are formed at the equator and break into small droplets before a bag gets a chance to form near the centre. Between these two asymptotic limits, when *We* is moderate, the drop can deform to a variety of shapes before breakup occurs (Jackiw & Ashgriz 2021). The variation in breakup morphology is very sensitive to *We* in the moderate range. As the drop is accelerated by the free stream, it experiences baroclinic torque and RTI on its windward side. Several models based on the linear stability analysis of RTI on a liquid layer of finite thickness (Mikaelian 1990, 1996) have been proposed to predict the critical Weber number (Joseph *et al.* 1999; Theofanous *et al.* 2004). However, the significance of the RTI, and whether the linear stability model captures the nonlinear development of the bag and the bag morphology change from a simple axisymmetric bag to more complex shapes, remain uncertain, despite its presence on the interface (Guildenbecher *et al.* 2009). It has been suggested that the Laplace pressure on the edge of the drop/disk contributes to hindering the bag formation or development (Guildenbecher *et al.* 2009), yet solid evidence to support the argument remains absent.

The goal of the present study is to investigate the aerobreakup of an isolated drop at moderate Weber numbers through detailed interface-resolved 3-D numerical simulation.

By using advanced numerical techniques, including the mass–momentum consistent volume-of-fluid method (Arrufat *et al.* 2020; Zhang, Popinet & Ling 2020), balanced-force surface tension discretization (Popinet 2009), and adaptive mesh refinement, we aim to resolve fully the two-phase turbulent interfacial flows involved in aerobreakup through large-scale parallel computations. The drop's initial diameter and fluid properties are kept unchanged, and the free-stream gas velocity is varied for a parametric study. Although typically the lateral radius of the drop increases monotonically in time (Flock *et al.* 2012; Opfer *et al.* 2014; Jackiw & Ashgriz 2021), the overall deformation is a complex process consisting of different phases with distinct features. The high-level details revealed by the simulation results will be used to identify the dominant mechanisms that dictate the deformation in each phase, and also to characterize the effect of *We*.

For the range of *We* considered, the drop will deform from its initial spherical shape to a forward bag with the opening facing the upstream direction. Although it is of great interest to study the rupture of thin bag sheets and the statistics of the droplets generated by the bag and rim breakups (Guildenbecher *et al.* 2017; Jackiw & Ashgriz 2022), the mesh resolution required to resolve fully the sheet rupture and hole formation is beyond the current available computational capability. If a liquid sheet breaks due to molecular forces, then the thickness must be reduced to tens of nanometres. For simulations of millimetre drops, a fully resolved simulation would need to cover over six orders of magnitude in length scales, which is obviously impractical even with today's computer power. Therefore, the present study will focus mainly on the drop deformation and bag formation and development before the bag sheet rupture occurs. The present simulations can be considered fully resolved and mesh-independent up to the early stage of the bag inflation, but not for the sheet rupture and child drop statistics. Nevertheless, the simulation results still provide important insights into the bag rupture mechanisms, such as the hole–hole interaction, which remain not fully understood. Since the occurrence of holes in the liquid sheet is random, ensemble averaging and statistics of multiple realizations (e.g. hole appearing locations and the number of holes) will be required to characterize fully the rupture dynamics and the statistics of the droplets formed (Mostert, Popinet & Deike 2022; Tang, Adcock & Mostert 2023), though such studies are outside the scope of the present work.

The rest of the paper will be organized as follows. Subsection 2.1 introduces the governing equations, and § 2.2 describes the numerical methods used in the present simulations. The physical parameters and simulation set-up are presented in § 2.3. Before discussing the simulation results, § 3 defines the characteristic length and time scales used to characterize the drop shape and gas flows. Grid-refinement and validation studies are presented in § 4. The simulation results identify different deformation phases, which are discussed in sequence in § 5. The effect of drop deformation on the aerodynamic drag and lift exerted on the drop is discussed in § 6. Finally, § 7 concludes the key findings of the present study.

2. Simulation methods

2.1. *Governing equations*

The two-phase interfacial flows are governed by the incompressible Navier–Stokes equations with surface tension,

$$\rho\left(\frac{\partial u_i}{\partial t}+u_i\frac{\partial u_j}{\partial x_j}\right)=-\frac{\partial p}{\partial x_i}+\frac{\partial}{\partial x_j}\left[\mu\left(\frac{\partial u_i}{\partial x_j}+\frac{\partial u_j}{\partial x_i}\right)\right]+\sigma\kappa\delta_s n_i, \tag{2.1}$$

$$\frac{\partial u_i}{\partial x_i} = 0, \tag{2.2}$$

where ρ, u_i, p, μ represent density, velocity vector, pressure and viscosity, respectively. The Dirac distribution function δ_s is localized on the interface. The surface tension coefficient σ is constant, and κ and n_i represent the curvature and normal vector of the interface.

The gas and liquid phases are distinguished by the liquid volume fraction c, the evolution of which follows the advection equation

$$\frac{\partial c}{\partial t} + u_i \frac{\partial c}{\partial x_i} = 0. \tag{2.3}$$

After spatial discretization, the cells with only liquid or gas will exhibit $c = 1$ and 0, respectively, while for cells containing the gas–liquid interface, $0 < c < 1$. The density and viscosity are both defined based on the arithmetic mean:

$$\rho = \rho_l c + \rho_g (1 - c), \tag{2.4}$$

$$\mu = \mu_l c + \mu_g (1 - c). \tag{2.5}$$

2.2. *Numerical methods*

The governing equations (2.1)–(2.3) are solved using the open-source, multiphase flow solver Basilisk. The Basilisk solver uses a finite-volume method for spatial discretization. The projection method is used to incorporate the incompressibility condition. The advection equation (2.3) is solved via a geometrical volume-of-fluid (VOF) method (Scardovelli & Zaleski 1999). The advection of momentum across the interface is conducted consistently with the VOF advection (Arrufat *et al.* 2020; Zhang *et al.* 2020). The mass–momentum consistency is essential for multiphase flows with large density contrast (Zhang *et al.* 2020). The balanced-force method is used to discretize the singular surface tension term in the momentum equation (Popinet 2009). The interface curvature required to calculate surface tension is computed based on the height-function method (Popinet 2009). The staggered-in-time discretization of the volume fraction/density and pressure leads to a formally second-order-accurate time discretization (Popinet 2009). An adaptive quadtree/octree mesh is used to discretize the computational domain, which allows adaptive mesh refinement in user-defined regions. The mesh adaptation is based on the wavelet estimate of the discretization errors of the liquid volume fraction and velocity (van Hooft *et al.* 2018). The parallelization of the solver is done through a tree decomposition to guarantee high parallel performance even if a large number of levels of octree cells are used. Numerous validation studies for the Basilisk solver can be found on the Basilisk website and also in our previous studies (Sakakeeny & Ling 2020, 2021; Zhang *et al.* 2020; Sakakeeny *et al.* 2021).

2.3. *Simulation set-up*

The spherical drop is initially placed in a computational domain filled with stationary gas. We have considered both 2-D-axisymmetric and 3-D domains, as shown in figures 1(*a*) and 1(*b*), respectively. At $t = 0^+$, a uniform velocity boundary condition (BC) is imposed on the left boundary of the domain, while the pressure outflow boundary condition is applied to the right boundary. Due to the incompressibility condition, the gas is suddenly accelerated to U_0 in an infinitesimal time (one time step in the simulation).

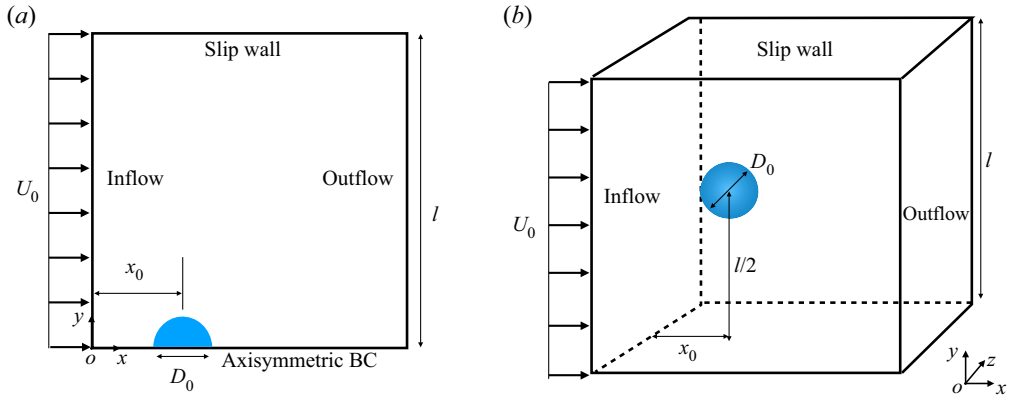

Figure 1. Schematics of the computational domains for (*a*) 2-D-axisymmetric and (*b*) 3-D simulations.

ρ_l (kg m^{-3})	ρ_g (kg m^{-3})	μ_l (Pa s)	μ_g (Pa s)	σ (N m^{-1})	d_0 (mm)	r ρ_g/ρ_l	m μ_g/μ_l	Oh $\mu_l/\sqrt{\rho_l D_0 \sigma}$
1000	1.2	0.001	0.000018	1.9	0.0483	0.0012	0.018	0.00269

Table 1. Fluid properties for simulation cases.

All lateral boundaries in the 3-D domain are considered as slip walls. For the 2-D domain, the bottom is the axis and the top is a slip wall. The 2-D domain is a square with edge length $l/d_0 = 16$, while the 3-D domain is a cube with edge length $l/d_0 = 32$. The domain size is sufficient to resolve the wake behind the drop during the time considered. For all 2-D and 3-D simulations, the drop is initially placed $x_0/d_0 = 3$ away from the inlet. In the 3-D simulations, the initial location of the drop is at the centre of the y–z cross-section.

The physical parameters used in the present simulations are chosen to be similar to the experiment of Jackiw & Ashgriz (2021). The liquid and gas are water and air at room temperature, and their fluid properties are given in table 1. The initial drop diameter is fixed at $d_0 = 1.9$ mm. The corresponding gas-to-liquid density and viscosity ratios are thus small, $r = 0.0012$ and $m = 0.018$, respectively. The Ohnesorge number $Oh = 0.0026$ is very small, indicating that the effect of liquid viscosity on drop breakup is small compared to that of surface tension, and the latter is the dominant force to resist the drop deformation/breakup induced by interaction with the gas stream. Therefore, the Weber number We is the key dimensionless parameter that characterizes the aerobreakup dynamics. A parametric study of We is performed here by varying U_0 from 18.7 to 24.0 m s^{-1}. The Reynolds number will vary from approximately 2400 to 3000 correspondingly. More cases were simulated, but we will focus the discussion on the five cases shown in table 2.

The 2-D/3-D domains are discretized by quadtree/octree meshes, which are adapted dynamically based on the wavelet estimates of the discretization errors of the liquid volume fraction and all velocity components (van Hooft *et al.* 2018). The minimum cell size is controlled by the maximum refinement level $\mathcal{L}$, i.e. $\Delta_{min} = l/2^{\mathcal{L}}$. For 2-D simulations, $\mathcal{L}$ has been varied from 12 to 15, corresponding to 256 to 2048 minimum quadtree

Case	U_0 (m s^{-1})	We $\rho_g U_0^2 d_0/\sigma$	Re $\rho_g U_0 d_0/\mu_g$	3-D mesh $N = d_0/\Delta_{min}$	2-D mesh N
1	18.7	10.9	2369	256	—
2	19.2	11.5	2432	256–2048	—
3	19.6	12.0	2483	256–2048	256–2048
4	22.1	15.3	2800	128–2048	—
5	24.0	18.0	3040	256–2048	—

Table 2. Simulation cases and key parameters.

cells across the initial drop diameter, i.e. $N = d_0/\Delta_{min} = 256$ to 2048. Due to the higher computational cost for 3-D simulations, we have used a different mesh adaptation strategy. As will be shown later, the mesh resolution required to capture the early deformation of the drop is significantly lower than that required to resolve the thin liquid sheet in the bag. Therefore, we have used a maximum refinement level $\mathcal{L} = 12$ to 14, which is equivalent to $N = 128$ or 512 to start the simulations, for the purpose of confirming that the resolution is enough to capture the drop deformation until the bag is formed. As the bag grows and the sheet thickness decreases, $\mathcal{L}$ is then increased up to 16 ($N = 2048$). For the case $We = 10.9$, since a thin bag sheet is never formed, $\mathcal{L} = 12$ ($N = 256$) is used throughout the simulation.

According to the knowledge of the authors, the current mesh resolution is significantly higher than all previous numerical studies, including both 2-D and 3-D simulations in the literature, while the domain is large enough to resolve the wake (Jain *et al.* 2019; Marcotte & Zaleski 2019). For the 3-D domain, the mesh for $N = 2048$ corresponds to 16 levels of adaptively refined octree cells, which is equivalent to 2.8×10^{14} uniform Cartesian cells. Generally, the total number of octree cells increases over time, as the drop surface area increases and the wake develops. For the case $We = 15.3$, the number of octree cells reaches approximately 500 million. The high-performance tree-decomposition parallelization technique in the Basilisk solver is essential to guarantee efficient simulations using such large numbers of levels (up to 16), computational cores (up to 3584), and octree cells (up to 500 million).

For the present study, the drop diameter is 1.9 mm, and the minimum cell size for $N = 2048$ is approximately $\Delta_{min} = 0.9$ μm, which is still significantly larger than the physical cutoff length scale dictated by van der Waals forces ($\sim O(10$ nm$)$). Therefore, the interfaces' pinching and hole formation induced by van der Waals forces will not be captured in the simulation. The hole nucleation in the liquid sheet here is due to the numerical cutoff length, i.e. the minimum cell size Δ_{min}. When the sheet thickness is smaller than approximately $2\Delta_{min}$, the flow and pressure in the liquid cannot be well resolved, and the thin region of the liquid sheet represented by the VOF field will be perturbed, and numerical pinching of the interfaces will occur. The numerical breakup leads to earlier hole formation, and as a result, the bag will break at a size smaller than what was observed in experiments. Nevertheless, as indicated in previous experimental studies, holes are observed in the liquid sheet with thickness larger than the length for active molecular forces (Lhuissier & Villermaux 2012; Opfer *et al.* 2014), probably due to tiny bubbles in the liquid sheet. A more detailed discussion of the effect of mesh resolution on the bag breakup dynamics will be given later, in the results section.

The 2-D simulations were run on the Baylor University cluster Kodiak using 4–36 cores (Intel Xeon Gold 6140 processor). The most refined simulation ($N = 2048$)

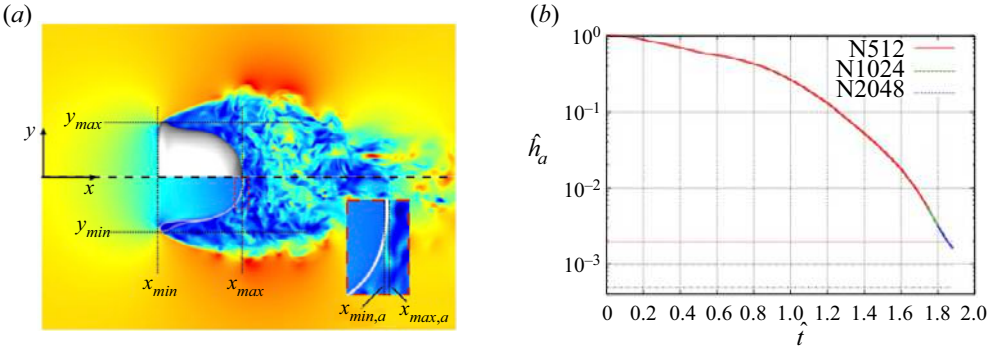

Figure 2. (*a*) Representative snapshot of the drop surface and velocity magnitude on the central x–y plane, with annotations showing the characteristic length scales for the drop shape. (*b*) Time evolution of $h_a = x_{max,a} - x_{min,a}$ for $We = 15.3$, indicating the time ranges resolved by different mesh resolutions. The horizontal lines indicate the minimum cell size for each mesh. The dimensionless variables are denoted by $\hat{\ }$, and defined in (3.10*a–e*) and (3.11).

takes approximately 20 days using 36 cores. The 3-D simulations were run on the TACC-Stampede2 (Intel Xeon Platinum 8160) and TACC-Frontera (Intel Xeon Platinum 8280) machines, using up to 3584 cores. The simulation time varies with cases, and the longest one takes approximately 50 days.

3. Parameters to characterize drop aerobreakup

Before we present and discuss the results, we will first introduce the parameters to be measured in the simulation to characterize the drop shape, dynamics and turbulent flows involved in the drop aerobreakup process.

3.1. *Drop morphology*

To characterize the drop shape at a given time, the maximum and minimum interfacial positions along the Cartesian coordinates were measured, i.e. x_{max}, x_{min}, y_{max}, y_{min}, z_{max}, z_{min}, as shown in figure 2(*a*). Furthermore, we also measured the maximum and minimum interfacial positions along the x-axis (along the streamwise direction), $x_{max,a}$, $x_{min,a}$. Based on these measurements, several characteristic length scales can be obtained.

(i) Length of the drop, $L = x_{max} - x_{min}$.

(ii) Lateral radius of the drop, $R = (y_{max} - y_{min} + z_{max} - z_{min})/4$. When the drop shape is axisymmetric, the maximum lateral radius is $R = y_{max} = -y_{min} = z_{max} = -z_{min}$; otherwise, R is the average for the y- and z-directions.

(iii) Thickness of the sheet along the x-axis, $h_a = x_{max,a} - x_{min,a}$. At early times, when the drop shape is axisymmetric and both windward and leeward sides are convex, $h_a = L$. At later times, when the drop deforms to a bag, h_a represents the sheet thickness at the centre of the bag, as shown in figure 2(*b*).

(iv) Length of the forward bag, $L_{fb} = x_{min,a} - x_{min}$. Here, 'forward bag' refers to the bag with the opening facing the upstream direction.

3.2. *Turbulent gas flow and drop dynamics*

For the range of *Re* considered, the gas flow in the wake of the drop lies in the chaotic vortex shedding or the subcritical turbulent wake regimes, according to the regime map for a solid sphere (Tiwari *et al.* 2020*b*). The gas enstrophy is then used to characterize the gas turbulence, which is calculated as

$$\Omega_g = \frac{1}{\mathbb{V}} \int (1 - c)\, |\boldsymbol{\omega}|^2 \, \mathrm{d}V, \tag{3.1}$$

where $\boldsymbol{\omega}$ is the vorticity vector, and $\mathbb{V}$ is the volume of the computational domain. The normalized gas enstrophy is defined as $\hat{\Omega}_g = \Omega_g d_0 / U_0^2$.

The aerodynamic drag exerted on the drop will cause the drop to accelerate along the streamwise direction. The mean velocity of the drop in the x-direction is calculated by integrating over all the liquid cells in the domain:

$$u_d = \frac{\int cu \, \mathrm{d}V}{\int c \, \mathrm{d}V}. \tag{3.2}$$

Note that this definition is valid only before breakup occurs. Then the drag coefficient can be defined as

$$C_D = \frac{2m_d}{\rho_g (U_0 - u_d)^2 \pi R^2} \frac{\mathrm{d}u_d}{\mathrm{d}t}, \tag{3.3}$$

where m_d is the mass of the drop. Here, C_D is defined based on the instantaneous relative velocity $(U_0 - u_d)$, and the drop frontal area is estimated by the lateral radius (πR^2). As a result, the variation of C_D is generally not influenced by the time variation of u_d and R.

The asymmetric drop deformation and the turbulent wake will introduce lift on the drop. The lift coefficients in the transverse directions are defined as

$$C_y = \frac{2m_d}{\rho_g (U_0 - u_d)^2 \pi R^2} \frac{\mathrm{d}v_d}{\mathrm{d}t}, \quad C_z = \frac{2m_d}{\rho_g (U_0 - u_d)^2 \pi R^2} \frac{\mathrm{d}w_d}{\mathrm{d}t}, \tag{3.4a,b}$$

where v_d and w_d are the mean drop velocities in the y- and z-directions, respectively, similar to u_d.

3.3. *Characteristic time scales for drop deformation*

The early-time deformation of the drop is driven by the pressure variation in the radial direction, which is in turn induced by the stagnation gas flow on the windward surface of the drop. The viscous and surface tension effects are secondary to the early-time deformation. Then simple scaling analysis shows that the time scale governing the drop deformation is (Ranger & Nicholls 1969; Villermaux & Bossa 2011)

$$\tau_d = \frac{d_0}{U_0 \sqrt{r}}. \tag{3.5}$$

The scaling $\tau_d \sim r^{-1/2}$ has been confirmed by the parametric study of Marcotte & Zaleski (2019). It was shown that the evolutions of R for different r collapse approximately if t is scaled by τ_d. This time scale τ_d was first introduced by Ranger & Nicholls (1969) based on the drag on the drop and the resulting acceleration. However, it was shown by Marcotte

& Zaleski (2019) that the time scale τ_d actually does not collapse the drop velocity for different r. In the present study, r and d_0 are kept constant, so τ_d varies due to U_0.

The surface tension and liquid viscosity resist the drop deformation, and the corresponding time scales are

$$\tau_s = \sqrt{\frac{\rho_l d_0^3}{\sigma}}, \tag{3.6}$$

$$\tau_{vl} = \rho_l d_0^2/\mu_l. \tag{3.7}$$

The time scale ratios are related to the key dimensionless parameters, i.e. $\tau_s/\tau_{vl} = Oh$ and $\tau_s/\tau_d = \sqrt{We}$. For the cases considered here, $Oh \sim O(10^{-3})$ is very small, and $We \sim O(10)$. As a result, $\tau_{vl} \gg \tau_s > \tau_d$. Therefore, τ_{vl} is too large to be relevant, and surface tension is the dominant resisting force. Furthermore, since $\tau_s > \tau_d$, we expect the early-time drop deformation will be insensitive to We.

3.4. *Characteristic time scales for drop acceleration*

When a stationary drop is suddenly exposed to the free stream, it experiences an impulsive gas acceleration and a continuous non-zero relative velocity. The resulting aerodynamic drag drives the drop to move along the streamwise direction. This treatment can be considered as an approximation of the passage of a shock wave with the post-shock velocity equal to U_0, neglecting the compressibility effect, as discussed by Marcotte & Zaleski (2019).

The overall drag can be divided into quasi-steady, pressure-gradient, added-mass and Basset history forces (Maxey & Riley 1983; Ling *et al.* 2013). The last three are unsteady contributions, which are triggered mainly by the impulsive acceleration. The pressure-gradient and added-mass forces, often referred to as the inviscid unsteady forces, are active only at $t = 0^+$, when the surrounding gas is suddenly accelerated from 0 to U_0. In the simulation, this impulse spans one time step, and the integration of the impulse is U_0. Therefore, the drop velocity jumps over the first time step due to the inviscid unsteady forces (including added-mass and pressure-gradient forces) as follows (Ling, Haselbacher & Balachandar 2011; Ling *et al.* 2013):

$$u_d(0^+) = \frac{3r}{2} U_0. \tag{3.8}$$

Similar estimates of the velocity jump have been proposed by Marcotte & Zaleski (2019) and Hadj-Achour *et al.* (2021). Marcotte & Zaleski (2019) found that the velocity jump scales with r, but the scaling coefficient $1/2$ is different from the $3/2$ in (3.8) since they did not include the pressure gradient force. The viscous-unsteady (Basset history) force will last for a finite period of time, characterized by the viscous-unsteady time scale τ_{vu} (Ling *et al.* 2013). Due to the small value of r considered here, the contributions of the unsteady forces to the increase in drop velocity are generally small (Ling *et al.* 2013). For cases with larger r, additional attention to the unsteady forces will be required. For the present cases, the quasi-steady force is the dominant force that accelerates the drop. The time scale for the quasi-steady drag is referred to as the response time, τ_{qs}. For $r \ll 1$ (Ling

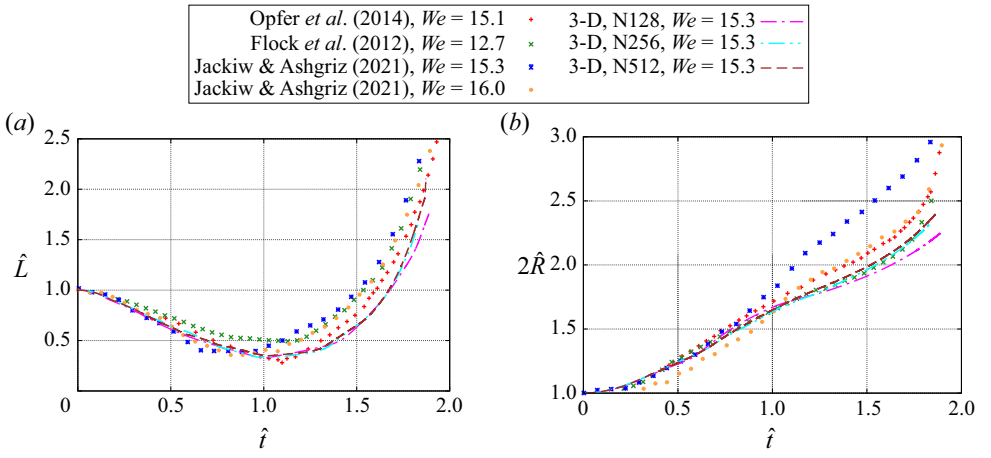

Figure 3. Time evolutions of (*a*) the drop length $\hat{L}$ and (*b*) the drop radius $\hat{R}$, for $We = 15.3$, obtained from the 3-D simulations. The experimental results by Opfer *et al.* (2014), Flock *et al.* (2012) and Jackiw & Ashgriz (2021) are shown for comparison.

et al. 2013),

$$\tau_{qs} = \frac{\rho_g d_0^2}{36\mu_g}\,\Phi, \tag{3.9}$$

where $\nu_g = \mu_g/\rho_g$, and Φ is the correction factor to the Stokes drag, accounting for the effect of Re and the drop shape. In the limit of zero Re and We, the drop acts like a solid sphere in the Stokes limit, and $\Phi = 1$. For the range of Re considered here, $\tau_{qs} \sim O(10^{-1}$ s). As a result, drop breakup occurs on a time scale much smaller than τ_{qs} when the drop velocity u_d remains significantly lower than the free-stream velocity U_0.

Finally, we define dimensionless variables using d_0, U_0 and ρ_g as characteristic scales, namely

$$\hat{x} = x/d_0, \quad \hat{L} = L/d_0, \quad \hat{R} = R/d_0, \quad \hat{u} = u/U_0, \quad \hat{p} = p/(\rho_g U_0^2). \tag{3.10a–e}$$

Due to the focus on the drop deformation, τ_d is selected as the characteristic time scale. The dimensionless time is then defined as

$$\hat{t} = t/\tau_d. \tag{3.11}$$

4. Verification and validation

4.1. *Grid-refinement studies*

The time evolutions of the drop length $\hat{L}$ and radius $\hat{R}$ for different mesh resolutions are shown in figure 3. The initial mesh resolutions are $N = 128$, 256 and 512. The same mesh refinement strategy has been used for all three meshes, i.e. when the drop deforms to a bag and the bag sheet thickness decreases to approximately 4 cells, refinement level will be increased until $N = 2048$, as shown in figure 2(*b*). It can be seen from figure 3 that the results for $N = 256$ and 512 match very well. The results for $N = 128$ are also similar in general, though small deviations are observed for $\hat{t} > 1.3$ when the forward bag forms. Therefore, one can conclude that $N = 512$ is sufficient to yield converged results for the

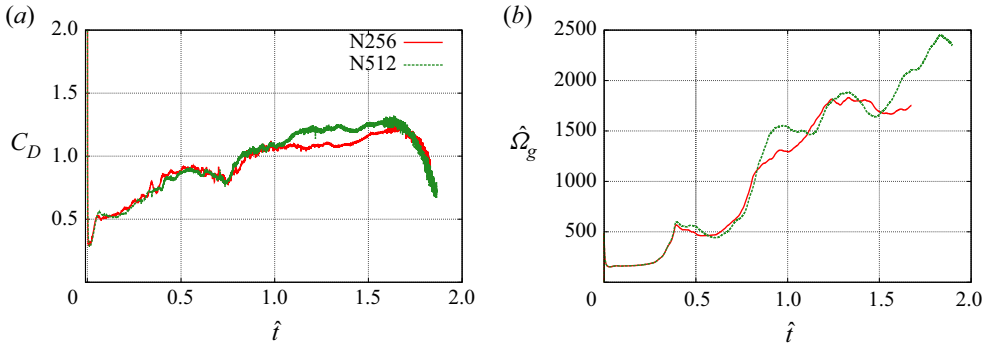

Figure 4. Time evolutions of (*a*) drag coefficient C_D and (*b*) gas enstrophy $\hat{\Omega}_g = \Omega_g d_0/U_0^2$ for $We = 15.3$. The 3-D simulation results for two different mesh resolutions, $N = 256$ and 512, are shown. In (*b*), the results for $N = 256$ were obtained by the mesh refinement $\mathcal{L} = 14$ without further increase, as in other cases.

drop deformation until the bag ruptures, and thus is sufficient to determine the breakup criteria.

In order to assess the adequacy of the mesh resolution in resolving the turbulent gas flow and its effect on the drag force, we examine the evolution of the drag coefficient C_D and the gas enstrophy (see figure 4). Both C_D and Ω_g exhibit non-monotonic behaviour due to the development of the turbulent wake and the drop deformation. The results obtained with meshes $N = 256$ and 512 show good agreement, with only minor discrepancies for $\hat{t} \gtrsim 1$. Given the inherently chaotic nature of the gas flow, this level of agreement is considered satisfactory.

4.2. *Experimental validation*

The simulation results obtained for the case $We = 15.3$ are validated against available experimental data for the drop length $\hat{L}$ and radius $\hat{R}$. Specifically, comparison is made with the experiments of Jackiw & Ashgriz (2021) (water, $We = 15.3$ and 16.0), Opfer *et al.* (2014) (ethylene glycol, $We = 15.1$), and Flock *et al.* (2012) (ethyl alcohol, $We = 12.7$). The parameters employed for the present simulations are chosen to be similar to those adopted in the experiments conducted by Jackiw & Ashgriz (2021) (JA). Although the dimensionless parameters for the two other experiments are not identical to those in the present study, the small values of Oh and r, and the large value of Re, in all cases suggest that the aerobreakup dynamics for similar We is expected to be comparable to the present cases. Thus the experimental data serve as an important validation benchmark for the present numerical simulations.

It can be observed from figure 3 that the simulation results for both $\hat{L}$ and $\hat{R}$ exhibit remarkable agreement with the experimental data of JA and Opfer *et al.* (2014) at early times. The deviations from the experimental results of Flock *et al.* (2012) are relatively small, given that the experimental parameters, such as $We = 12.7$, do not match the present simulations exactly. The simulation results for $\hat{R}$ deviate from the JA experimental data for the same $We = 15.3$ at approximately $\hat{t} = 0.7$, but they match quite well with the JA experimental results for a slightly larger $We = 16$ and the other two experiments. The discrepancy may be due to the high degree of variation inherent in such experiments. Unlike the results of Opfer *et al.* (2014) and Flock *et al.* (2012), which are averaged data for multiple experiments, those of JA correspond to single experimental runs and thus exhibit

higher uncertainty. Moreover, in JA's experiment, the drop is suspended from a needle, which may significantly influence the development of the drop radius, as discussed in the appendix of their paper.

4.3. *Limitations of 2-D axisymmetric simulations*

Due to the high computational cost of 3-D simulations, 2-D axisymmetric simulations have been used widely in numerical studies of drop aerobreakup (Jain *et al.* 2019; Marcotte & Zaleski 2019; Stefanitsis *et al.* 2019*a*). However, previous studies for bubbles (Blanco & Magnaudet 1995; Magnaudet & Mougin 2007) and drops (Rimbert *et al.* 2020) have also indicated that 2-D axisymmetric simulations may not be sufficient to resolve the asymmetric wake when *Re* and *We* are not small. It remains unclear to what extent (such as time duration and ranges of *Re* and *We*) a 2-D axisymmetric simulation is valid in resolving drop aerobreakups. In the present study, we have performed both 2-D and 3-D simulations using identical numerical methods and initial/boundary conditions. Therefore, the difference between the results characterize the effect of the artificial axisymmetric constraint in the 2-D simulations on the drop.

The temporal evolutions of $\hat{L}$ and $\hat{R}$ for both 2-D and 3-D simulations are shown in figure 5. The 2-D simulation results for two different mesh resolutions, $N = 512$ and $N = 1024$, agree remarkably well, indicating that the 2-D results presented here are mesh-independent. The discrepancy between the 2-D and 3-D results is not related to the mesh resolution. The 2-D and 3-D results match very well for $\hat{t} \lesssim 0.5$, but the deviation grows over time. In general, the 3-D results agree much better with the experimental data. The 2-D simulation significantly underestimates the drop length compared to the 3-D simulation and experimental results, as shown in figure 5(*a*). This indicates that the 2-D simulations fail to capture the bag development. Significant discrepancies can also be observed in the drop velocity and drag coefficient, as shown in figures 5(*c*) and 5(*d*). For $1 \lesssim \hat{t} \lesssim 1.6$, the value of C_D predicted by the 2-D simulation is only approximately half of that obtained from the 3-D simulation.

The poor prediction of the 2-D simulation is due to the fact that it cannot resolve the turbulent wake accurately. The pressure fields obtained from both 2-D and 3-D simulations are shown in figures 6(*a*) and 6(*b*), respectively. The vortical structures at different times for the 3-D simulation, visualized by the λ_2 criterion, are shown in figure 6(*c*) to illustrate the development of the wake. The wake is initially approximately axisymmetric and later transitions to being fully 3-D and turbulent. The artificial axisymmetric constraint in the 2-D simulation limits the azimuthal development of the wake, leading to high pressure near the leeward pole and a low-pressure region in the symmetric vortex ring, as seen in figure 6(*a*) at $\hat{t} = 0.78$. In contrast, the gas pressure near the leeward pole is lower and more uniform in the turbulent wake for the 3-D results. The different pressure distributions result in different drags on the drop. The high pressure on the leeward pole in the 2-D simulation also hinders the development of the bag, which is the reason for the discrepancy for $\hat{L}$ observed in figure 5(*a*). Actually, the 2-D simulation fails to capture the correct shape of the bag, as seen at $\hat{t} = 1.76$ in figures 6(*a*) and 6(*b*). While the 3-D simulation shows a bag curved forward shape, the 2-D bag bends upstream near the centre, showing a 'bag-stem' shape. The maximum bag curvature and minimum sheet thickness in the 2-D bag are near the 45-degree corner, where the rupture of the bag and the hole will appear first. This is

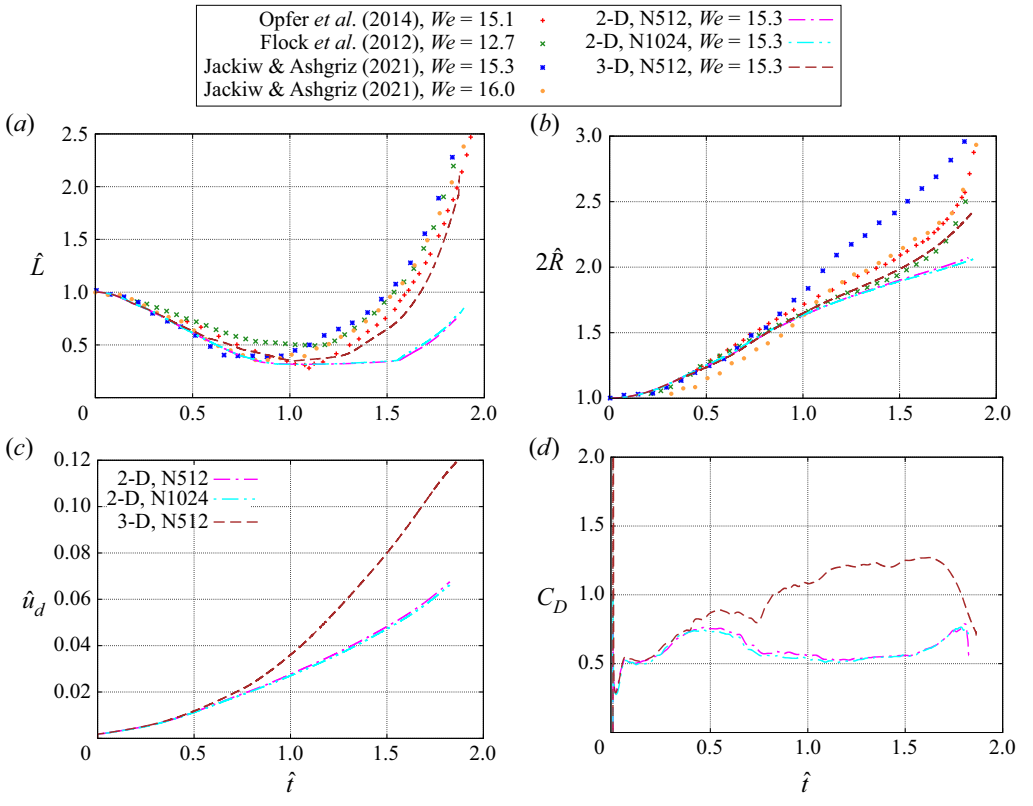

Figure 5. Comparison between 2-D-axisymmetric and 3-D simulation results for $We = 15.3$, including (*a*) drop length $\hat{L}$, (*b*) drop radius $\hat{R}$, (*c*) drop velocity u_d, and (*d*) drag coefficient C_D. The experimental results by Opfer *et al.* (2014), Flock *et al.* (2012) and Jackiw & Ashgriz (2021) are shown in (*a*,*b*) for comparison.

not consistent with the experiment and 3-D simulation results, and is purely a numerical artefact.

In summary, for drops with high *Re*, the 2-D simulation can capture only the early-time drop dynamics and deformation ($\hat{t} \lesssim 0.7$), when the wake remains approximately axisymmetric. Even though the drop shape for $We = 15.3$ remains approximately axisymmetric for a longer time, it will not be captured correctly by the 2-D axisymmetric simulation. A full 3-D simulation, though expensive, is necessary to resolve the drop aerobreakup.

5. Different phases in drop morphological evolution

The shape deformation of a drop is a complex process consisting of multiple phases with distinct features and dominant physics. We will use the case $We = 12.0$ to illustrate the different deformation phases, as shown in figure 7. In figures 7(*a*) and 7(*b*), we have presented the temporal evolution of pressure $\hat{p}$ and y-velocity $\hat{u}_y$ inside the drop on the central x–y plane. The corresponding drop surfaces, coloured with the velocity magnitude, are shown in figure 7(*c*). The drop radius $\hat{R}$ has been used commonly in previous studies to describe drop deformation, and it increases monotonically over time. However, its rate of

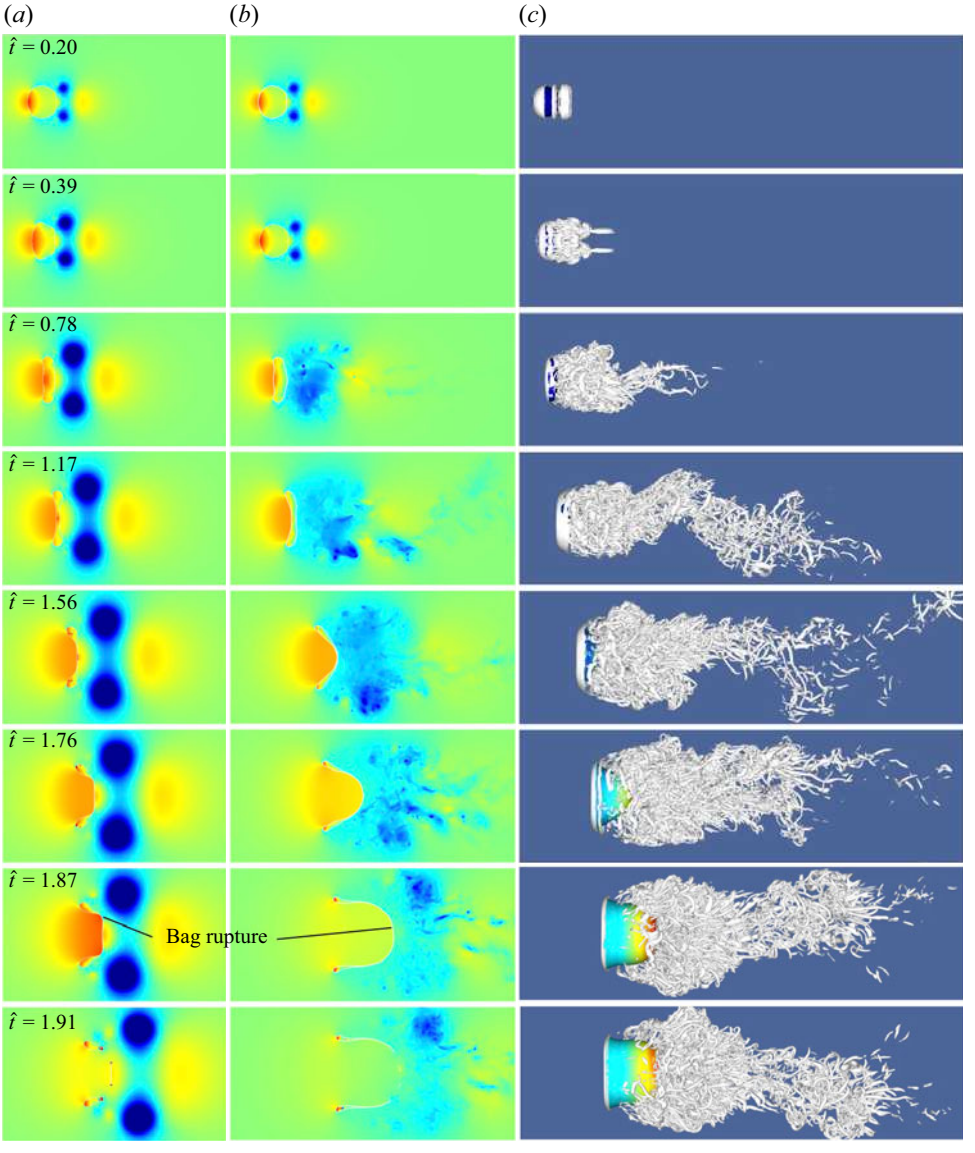

Figure 6. Time evolutions of the pressure field on the x–y plane using (*a*) 2-D-axisymmetric and (*b*) 3-D simulations. (*c*) Vortical structures using 3-D simulations. The results are for the case $We = 15.3$. The colour on the drop surface in (*c*) represents the velocity magnitude. See movies in the supplementary materials available at https://doi.org/10.1017/jfm.2023.708.

change $\mathrm{d}\hat{R}/\mathrm{d}\hat{t}$ exhibits a non-monotonic variation over time, as shown in figure 7(*d*), from which different phases can be identified.

(i) Phase I, ellipsoid deformation: $\mathrm{d}\hat{R}/\mathrm{d}\hat{t}$ increases over time with a decreasing rate and gradually approaches a plateau. The deformation is driven by the stagnation pressure on the windward surface. The drop shape is similar to an ellipsoid, and the thickness in the streamwise direction decreases over time.
(ii) Phase II, disk formation: $\mathrm{d}\hat{R}/\mathrm{d}\hat{t}$ rises quickly again as the drop extends laterally, forming a circular disk.

(iii) Phase III, disk deformation: $\mathrm{d}\hat{R}/\mathrm{d}\hat{t}$ decreases over time. The deceleration of the drop edge and equator is due to surface tension at the drop periphery.

(iv) Phase IV, bag development: $\mathrm{d}\hat{R}/\mathrm{d}\hat{t}$ is approximately constant, indicating that forces reach equilibrium at the edge rim. The sheet thickness near the centre continues to decrease, and the thin region of the bag starts to curve toward downstream, forming a forward bag.

(v) Phase V, bag inflation: $\mathrm{d}\hat{R}/\mathrm{d}\hat{t}$ increases rapidly due to the inflation of the forward bag.

After the above phases, there is an additional phase, phase VI, for the bag rupture, which is not shown in figure 7. These phases have not been addressed systematically in previous studies, probably because little attention has been paid to the evolution of $\mathrm{d}\hat{R}/\mathrm{d}\hat{t}$. The key features of drop deformation in each phase and the effect of *We* will be discussed in subsequent subsections.

5.1. *Phase I: ellipsoid deformation*

In phase I, the windward surface remains convex, so $L_{fb} = 0$. Stagnation flows are formed near the windward and leeward poles (see points W and L in figure 7*a*). On the windward surface, the gas pressure is high near the stagnation point and decreases along the surface in the lateral direction. If the viscous effect is ignored, then the gas pressure near the stagnation point is given as

$$p_g(r) = p_g(0) - \rho_g \frac{a^2 U^2}{8 d_0^2} r^2, \tag{5.1}$$

where r is the radial coordinate from the x-axis. The stretching rate of the stagnation flow, a, varies with the shape of the windward surface geometry, e.g. $a = 6$ for a spherical surface, and $a = \pi/4$ for a flat disk (Villermaux & Bossa 2009). The liquid pressure inside the drop can be estimated as the sum of the gas pressure and the Laplace pressure,

$$p_l(r) = p_g(r) + \sigma\kappa, \tag{5.2}$$

which exhibits a variation in r similar to that for p_g. The gradient of p_l drives the extension of the drop in the radial direction, as shown in figure 7(*b*) at $\hat{t} = 0.14$. If the liquid flow is modelled as one-dimensional and inviscid (due to the low *Oh* for the present cases), then the momentum equation can be expressed as

$$\rho_l \left(\frac{\partial u_r}{\partial t} + u_r \frac{\partial u_r}{\partial r} \right) = -\frac{\partial p_l}{\partial r}, \tag{5.3}$$

which can be integrated from $r = 0$ to R to yield

$$R \frac{\mathrm{d}^2 R}{\mathrm{d}t^2} = \frac{2(p_l(0) - p_l(R))}{\rho_l}. \tag{5.4}$$

Combining (5.2), an evolution equation for $\hat{R}$ can be obtained (Villermaux & Bossa 2009; Kulkarni & Sojka 2014; Jackiw & Ashgriz 2021):

$$\frac{\mathrm{d}^2 \hat{R}}{\mathrm{d}\hat{t}^2} \frac{1}{\hat{R}} = \left(\frac{a}{2}\right)^2 \left[1 - \frac{8}{a^2\, We} \frac{\hat{\kappa}_E - \hat{\kappa}_W}{\hat{R}^2} \right], \tag{5.5}$$

where $\hat{\kappa}_W$ and $\hat{\kappa}_E$ are the curvatures at the windward pole ($r = 0$, point W) and the lateral edge ($r = \hat{R}$, point E).

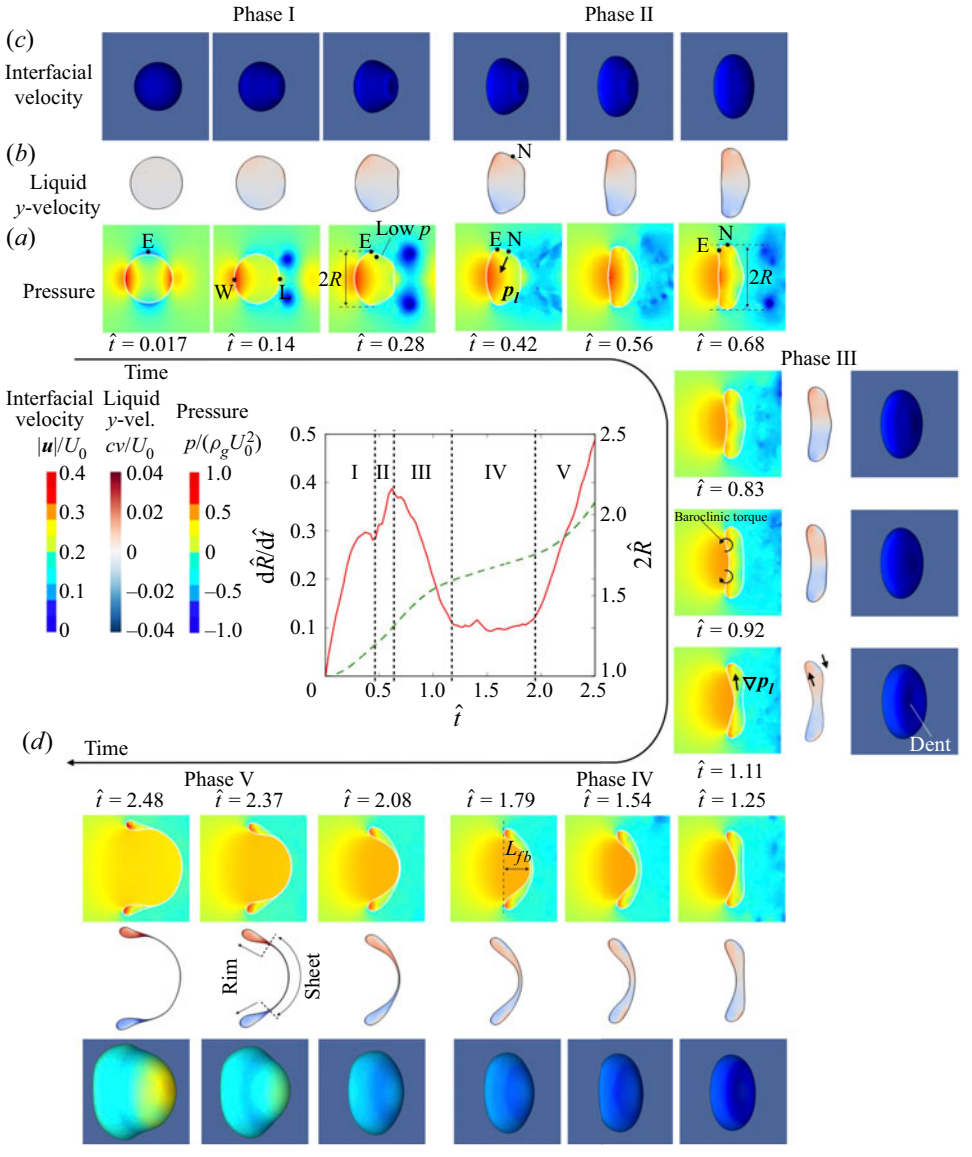

Figure 7. Temporal evolutions of (*a*) pressure p and (*b*) y-velocity in the drop on the central x–y plane. (*c*) Drop surface coloured with velocity magnitude. (*d*) Drop lateral radius $\hat{R}$ and its rate of change $\mathrm{d}\hat{R}/\mathrm{d}\hat{t}$ for $We = 12.0$. Different phases of deformation are defined and indicated.

5.1.1. *Asymptotic early-time dynamics*

At $t = 0$, $\hat{\kappa}_W = \hat{\kappa}_E = 1/\hat{R}0$, so (5.5) reduces to

$$\left(\frac{\mathrm{d}^2\hat{R}}{\mathrm{d}\hat{t}^2}\right)_{t=0} = \frac{a^2}{8}, \tag{5.6}$$

indicating that the drop deformation in the asymptotic limit is independent of We and is determined purely by a. This universal early-time behaviour is consistent with the time scale analysis above (i.e. $\tau_{vl} \gg \tau_s > \tau_d$) and is also confirmed by the simulation results;

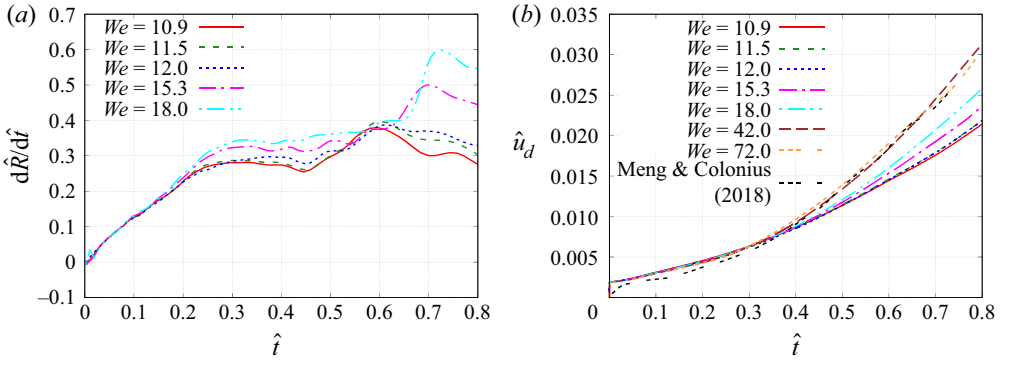

Figure 8. Early-time evolution of (*a*) rate of change of drop radius $\mathrm{d}\hat{R}/\mathrm{d}\hat{t}$ and (*b*) drop velocity $\hat{u}_d$, for different *We*. The inviscid compressible flow simulation results for shock–droplet interaction by Meng & Colonius (2018) are shown in (*b*) for comparison.

see figure 8. It is observed that $\mathrm{d}\hat{R}/\mathrm{d}\hat{t}$ for all cases collapses very well at early times ($\hat{t} \lesssim 0.15$) for the range of *We* considered ($10.9 \leq We \leq 18$).

Similarly, the results for the drop velocity u_d also collapse in the early time ($\hat{t} \lesssim 0.3$); see figure 8(*b*). The initial jump of u_d at $t = 0^+$ is observed, which is due to the impulsive gas acceleration and the resulting inviscid-unsteady forces. Therefore, the velocity jump is also independent of *We* and *Re*. The velocity jump $\hat{u}(t = 0^+) \approx 0.002$ agrees well with the prediction given by (3.8). The results from the inviscid compressible flow simulation of Meng & Colonius (2018) are also shown for comparison. In their simulations, the stationary water drop is hit by a planar air shock of Mach number $M_s = 1.47$. Due to the compressibility effect, the drop velocity 'jump' occurs in a finite period of time ($\hat{t} \lesssim 0.04$). Nevertheless, the subsequent evolution of u_d agrees well with the present simulations, assuming incompressible flows. The good agreement affirms that the early-time drop dynamics for the ranges of *We* and *Oh* considered is independent of viscous and surface tension effects.

5.1.2. *Effect of We*

The inviscid results of Meng & Colonius (2018) deviate from the present cases at later times $\hat{t} \gtrsim 0.3$ due to the effect of surface tension. Additional 3-D simulations were performed for higher *We*, and it is shown that the present simulation results for $We = 42$ and 72 agree well with the results of the inviscid simulation results for the whole time range shown. This indicates that the compressibility effect on drop breakup induced by weak shocks on the drop velocity is secondary, and the incompressible flow simulations can yield a reasonable estimate for shock-induced drop aerobreakup.

Deviations among different cases for $\mathrm{d}\hat{R}/\mathrm{d}\hat{t}$ arise after approximately $\hat{t} = 0.2$, as shown in figure 8(*a*). It can be observed that $\mathrm{d}\hat{R}/\mathrm{d}\hat{t}$ for different *We* eventually reaches different plateau values. As the curvatures of the windward surface decrease, the stagnation flow is modified, and the pressure gradient that drives the lateral expansion is reduced. Simultaneously, the curvature at the lateral edge increases, and as a result, the retraction force due to surface tension increases. The balance between the surface tension and stagnation pressure brings $\mathrm{d}\hat{R}/\mathrm{d}\hat{t}$ to a constant. For cases with larger *We*, the retraction force from the lateral edge is smaller, thus it takes slightly longer for $\mathrm{d}\hat{R}/\mathrm{d}\hat{t}$ to reach the plateau, and the plateau values of $\mathrm{d}\hat{R}/\mathrm{d}\hat{t}$ are also higher.

The above discussions focus mainly on the windward surface. Due to flow separation, the pressure field on the leeward side is different from the windward counterpart, as shown in figure 7(*a*). Generally, the pressure at the leeward pole is lower. Nevertheless, the pressure decreases radially even faster due to the vortex ring formed behind the separation point. As a result, the leeward surface curvature decreases faster and turns from convex to concave earlier ($\hat{t} = 0.28$) than the windward counterpart.

5.1.3. *Modelling early-time evolution of drop radius R*

The evolution of the drop radius R is dictated mainly by windward surface deformation. The shape of the drop can be approximated as ellipsoidal. Then κ_W and κ_E can be expressed in terms of R as $\kappa_W = h_a/R^2$ and $\kappa_E = 4R/h_a^2 + 1/R$, where $h_a = d_0^3/4R^2$ is the thickness of the drop for an ellipsoid. By substituting the estimates of curvatures into (5.5), we obtain

$$\frac{\mathrm{d}^2\hat{R}}{\mathrm{d}\hat{t}^2}\,\frac{1}{\hat{R}} = \left(\frac{a}{2}\right)^2\left[1 - \frac{64}{a^2\,We}\left(8\hat{R}^3 + \frac{1}{8\hat{R}^3} - \frac{1}{32\hat{R}^6}\right)\right]. \tag{5.7}$$

Similar models have been developed by Villermaux & Bossa (2009) (VB) and were then extended by Kulkarni & Sojka (2014) (KS) and Jackiw & Ashgriz (2021) (JA). The difference between the present model (5.7) and the previous ones lies in the different estimates of κ_W and κ_E. In the VB and KS models, the drop is assumed to be a cylindrical disk with a rounded edge, so the windward surface is flat ($\kappa_W = 0$), and only the principal curvature on the x–y plane is considered for the edge, namely $\kappa_E = 2/h_a$, where $h_a = d_0^3/6R^2$ for a cylinder. As a result, (5.5) becomes

$$\left(\frac{\mathrm{d}^2\hat{R}}{\mathrm{d}\hat{t}^2}\,\frac{1}{\hat{R}}\right)_{KS} = \left(\frac{a}{2}\right)^2\left[1 - \frac{96}{a^2\,We}\right]. \tag{5.8}$$

Note that this expression holds for both the VB and KS models; the difference between the two lies in the different values of a. In the JA model, the drop was first considered as a disk, so $\kappa_W = 0$ and $\kappa_E = 2/h_a + 1/R$, with the second principal curvature added compared to the KS model. Nevertheless, when relating h_a to R, they have used the relation for an ellipsoid, so $h_a = d_0^3/4R^2$. Eventually, they obtained

$$\left(\frac{\mathrm{d}^2\hat{R}}{\mathrm{d}\hat{t}^2}\,\frac{1}{\hat{R}}\right)_{JA} = \left(\frac{a}{2}\right)^2\left[1 - \frac{64}{a^2\,We}\left(1 + \frac{1}{8\hat{R}^3}\right)\right]. \tag{5.9}$$

Based on experimental observations, they argued that for a short time $\hat{t} < \hat{t}_{bal} = 1/8$, the drop radius R remains unchanged, and then R increases linearly. Therefore, (5.9) can be simplified further as

$$\left(\frac{\mathrm{d}\hat{R}}{\mathrm{d}\hat{t}}\right)_{JA2} = \begin{cases} 0, & \text{if } \hat{t} \le \hat{t}_{bal}, \\ \left(\dfrac{a}{2}\right)^2\left[1 - \dfrac{128}{a^2\,We}\right]\dfrac{\hat{t}_{bal}}{2}, & \text{if } \hat{t} > \hat{t}_{bal}, \end{cases} \tag{5.10}$$

which is referred to as the JA2 model here, to distinguish it from (5.9). In the present model, we have used the geometric features of an ellipsoid to estimate κ_W, κ_E, and the relation between h_a and R consistently. This treatment leads to an important feature, the

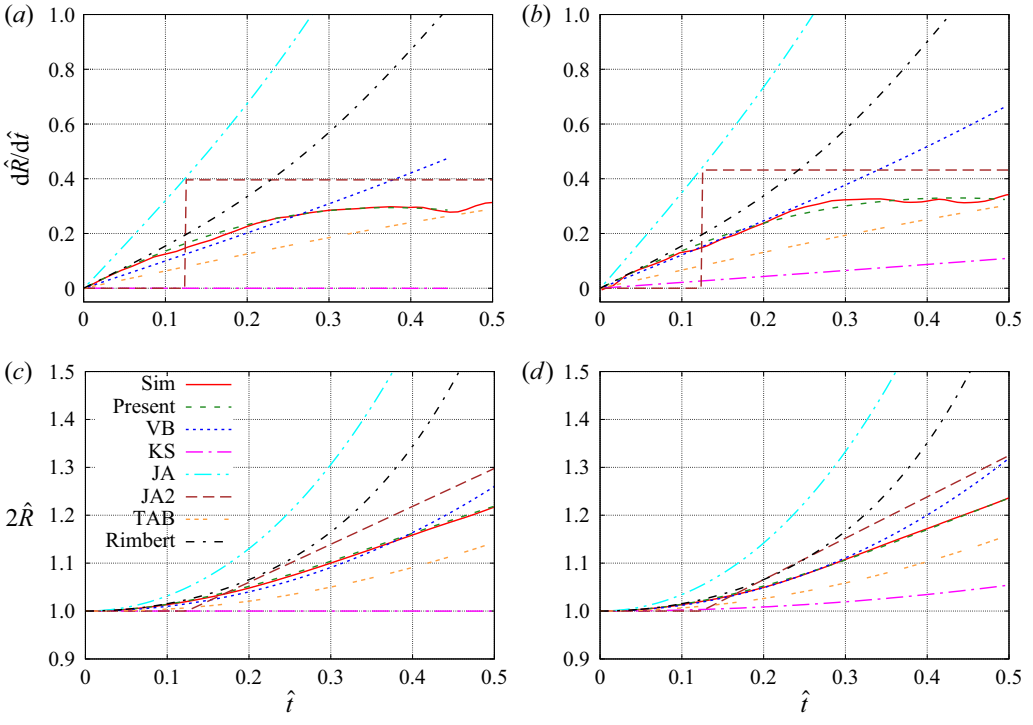

Figure 9. Comparison between the present simulation and model results for $d\hat{R}/d\hat{t}$ and $\hat{R}$ and predictions of other models for (*a*,*c*) $We = 12.0$ and (*b*,*d*) $We = 15.3$. The results for other models are shown as well: VB, KS, TAB, Rimbert represent the models of Villermaux & Bossa (2009), Kulkarni & Sojka (2014), O'Rourke & Amsden (1987) and Rimbert *et al.* (2020); JA and JA2 represent the two models of Jackiw & Ashgriz (2021) ((5.9) and (5.10)). The results for the model of Rimbert *et al.* (2020) are based on the corrected parameter K_C. Refer to the text for more details.

We-independent asymptotic limit at $t = 0$ (see (5.6)), being captured correctly. It can be shown easily that none of the above models guarantees this feature.

To close the above models, the stretching rate of the stagnation flow, a, remains to be determined. In the VB model, a is taken to be 4, which is an arbitrary intermediate chosen between the two limits $a = 6$ and $\pi/4$ for sphere and cylinder. Both VB and KS proposed that the condition $d^2R/dt^2 = 0$ can be used to determine the critical Weber number We_{cr}; i.e. when $We < We_{cr}$, $d^2R/dt^2 < 0$, then R will not increase over time and the drop will be stable. The value $a = 4$ used by VB will lead to $We_{cr} = 6$, which does not agree with experimental observations for drop aerobreakup. That is why KS proposed $a = 2\sqrt{2}$, so that according to their model (5.8), $d^2R/dt^2 = 0$ will yield $We_{cr} = 12$, which agrees with the experimental observations. Nevertheless, this way to estimate a is problematic since both experimental and simulation results show that $d^2R/dt^2 > 0$ is not a necessary condition for the drop to be unstable. A good counterexample is the case $We = 10.9$, for which $d^2R/dt^2 > 0$ at an early time. However, the drop is eventually stable. Generally, the KS model significantly underpredicts the temporal growth of R at an early time; see figures 9(*b*) and 9(*d*). In particular, for the case $We = 12.0$, the KS model will yield $d^2R/dt^2 = 0$, and as a result, R would not grow in time (see figures 9*a*,*c*), which is obviously incorrect.

In the JA model, the value of a for a sphere was used, i.e. $a = 6$. In contrast to the KS model, the JA model significantly overpredicts the evolution of $\hat{R}$ and $\mathrm{d}\hat{R}/\mathrm{d}\hat{t}$. Among the VB, KS and JA models, the VB model actually matches the best with the present simulation results for the initial development of $\hat{R}$ and $\mathrm{d}\hat{R}/\mathrm{d}\hat{t}$ for $\hat{t} \lesssim 0.25$. Nevertheless, a common issue of all these models is that they fail to capture the trend that $\mathrm{d}\hat{R}/\mathrm{d}\hat{t}$ gradually reaches a plateau at $\hat{t} \approx 0.3$. The constant $\mathrm{d}\hat{R}/\mathrm{d}\hat{t}$ was observed in the experiments of JA, which motivated them to add this assumption in the original JA model, leading to the simplified JA2 model that approximates $\mathrm{d}\hat{R}/\mathrm{d}\hat{t}$ as a piecewise constant function of time; see (5.10). This simplification reduces the discrepancy between the model predictions and the simulation results. However, as shown in figures 9(*a*,*b*), the evolution of $\mathrm{d}\hat{R}/\mathrm{d}\hat{t}$ in reality does not change abruptly.

In a recent study by Rimbert *et al.* (2020), the potential flow solution around a spheroid was used to estimate the gas pressure on the drop surface. Therefore, their model does not require *ad hoc* models for the stagnation flow features, such as the stretching rate of the stagnation flow, a, and the time-varying pressure work on the drop is expressed as a function of $\hat{R}$. The drop deformation in time is determined through an energy approach, namely the time derivative of the sum of kinetic and surface energy is equal to the pressure and viscous works. In the original paper, the authors seem to have missed a factor $1/2$ in the kinetic energy parameter K_C. The predictions of the model by Rimbert *et al.* (2020) with the corrected K_C are shown in figure 9. It can be observed that the model agrees remarkably well with the present simulation results at early times, though it generally overpredicts the evolutions of $\mathrm{d}\hat{R}/\mathrm{d}\hat{t}$ and $\hat{R}$ at later times when the drop deviates from the spheroidal shape.

By introducing a small perturbation at the initial spherical state, $\hat{\epsilon} = 2\hat{R} - 1$, the model of Rimbert *et al.* (2020) (with corrected K_C) can be simplified to a linear form, i.e.

$$\frac{\mathrm{d}^2\hat{\epsilon}}{\mathrm{d}\hat{t}^2} + 40\,\frac{Oh}{\sqrt{We}}\,\frac{\mathrm{d}\hat{\epsilon}}{\mathrm{d}\hat{t}} + \left(\frac{64}{We} - \frac{684}{35}\right)\hat{\epsilon} = 3. \tag{5.11}$$

The constant 3 on the right-hand side is determined by the pressure work of the gas flow, estimated from the potential flow solution, and the kinetic energy within the liquid drop. At time zero, $\hat{\epsilon} = \mathrm{d}\hat{\epsilon}/\mathrm{d}\hat{t} = 0$, so we have

$$\left(\frac{\mathrm{d}^2\hat{\epsilon}}{\mathrm{d}\hat{t}^2}\right)_{t=0} = 3, \quad \text{or} \quad \left(\frac{\mathrm{d}^2\hat{R}}{\mathrm{d}\hat{t}^2}\right)_{t=0} = \frac{3}{2}, \tag{5.12}$$

which yields an analytical solution for the initial slope of $\mathrm{d}\hat{R}/\mathrm{d}\hat{t}$, i.e. $(\mathrm{d}\hat{R}/\mathrm{d}\hat{t})_{t=0} = 3/2$. Consistent with (5.6), the model of Rimbert *et al.* (2020) also indicates that the initial slope of $\mathrm{d}\hat{R}/\mathrm{d}\hat{t}$ is independent of *We* and *Oh*.

To predict the evolution of $\hat{R}$ in phase I, a simple model is proposed here by incorporating a time varying a. First, by combining (5.6) and (5.12), one can determine the initial value of a, i.e. $a_0 = a(t = 0) = \sqrt{(\mathrm{d}^2R/\mathrm{d}t^2)_{t=0}} = \sqrt{12}$. The value is lower than 6 even though the initial drop shape is spherical, and the difference is related to the simplified pressure distribution on the drop surface, i.e. (5.1). As the drop deforms and the windward surface curvature decreases, a decreases over time and eventually reaches a_1. The time

variation of a is modelled simply by an error function as

$$a = a_0 - (a_0 - a_1)\,\mathrm{erf}(\hat{t}/\hat{\tau}_a), \tag{5.13}$$

where $a_1 = 2.5$ is the asymptotic value of a at the end of phase I, and $\tau_a = 0.35$ is the transition time, found based on the simulation results. Though the present model ((5.7) and (5.13)) requires simulation results to calibrate the model parameters, (5.13) is independent of *We* and thus can be used to predict the evolution of R in phase I for other values of *We* that are not simulated here. It is also worth noting that previous models (except JA2) predict continuous growth of $\mathrm{d}\hat{R}/\mathrm{d}\hat{t}$, which is inconsistent with the present simulation results and experimental data of Jackiw & Ashgriz (2021). By using a decaying a, the present model agrees very well with the simulation results; see figures 9(*a*) and 9(*b*).

Finally, as the TAB model (O'Rourke & Amsden 1987) is used widely in the literature, its results are also shown in figure 9 for comparison. It can be observed that the TAB model underpredicts the initial growths of $\mathrm{d}\hat{R}/\mathrm{d}\hat{t}$ and $\hat{R}$.

5.2. *Phase II: disk formation*

A distinct feature of phase II is that $\mathrm{d}\hat{R}/\mathrm{d}\hat{t}$ increases again after it reaches the plateau at the end of phase I, as shown in figure 7(*d*). As shown in figure 7(*a*), as the pressure at point E increases, the growth of $\mathrm{d}\hat{R}/\mathrm{d}\hat{t}$ slows down at the end of phase I. In phase II, the liquid turns to flow towards a new low-pressure location, the point N marked in the figure. The low pressure is related to small curvature at point N on the x–y plane, which is in turn related to the deformation of the leeward surface in phase I. It can be observed that the y-velocity at point N increases faster than that at point E, as shown for $\hat{t} = 0.42$ to 0.68 in figure 7(*b*). As a result, the lateral extension velocity of the drop increases again. At approximately $\hat{t} = 0.56$, the point N passes the point R, becoming the new location determining R. As the drop deforms, the curvature at point N increases, and the drop gradually deforms from an approximate ellipse to a disk with rounded edge. At the end of phase II, the Laplace pressure at the new periphery N becomes comparable to the stagnation pressure near the windward pole. Then $\mathrm{d}^2\hat{R}/\mathrm{d}\hat{t}^2 = 0$, and $\mathrm{d}\hat{R}/\mathrm{d}\hat{t}$ reaches a local maximum.

It is worth mentioning that the model given in (5.5) can also be used to predict the drop deformation in this phase, with certain adaptation. The additional complexity is to estimate the time variation of the principal curvature κ_N on the x–y plane since the shape of the drop is neither an ellipse nor a disk in the transition. In this study, we focus on discussions of the flow physics and will leave the model development for future work.

The appearance of a local maximum in $\mathrm{d}\hat{R}/\mathrm{d}\hat{t}$ is a distinctive feature of the bag breakup regime. As *We* increases and the drop breakup mode transitions to the multi-mode regime, $\mathrm{d}\hat{R}/\mathrm{d}\hat{t}$ will increase monotonically. Here, we denote the time corresponding to $\mathrm{d}^2\hat{R}/\mathrm{d}\hat{t}^2 = 0$ in phase II as $\hat{t}^*$. The zero acceleration of $\hat{R}$ indicates a force balance at the drop periphery. When *We* is too large, the surface tension will not be sufficient to establish such a balance. Marcotte & Zaleski (2019) suggested that the force balance at the drop periphery is achieved when the rim is formed, which is consistent with the present results. They also suggested that rim formation is a critical feature in determining whether the drop will break in the bag modes (Rayleigh–Taylor piercing mode) or in the shear modes (shear-induced entrainment mode). Nevertheless, the present results show that rim formation will not be achieved even in the multi-mode regime, and that *We* does not need to reach high values in the shear breakup regime to prevent rim formation.

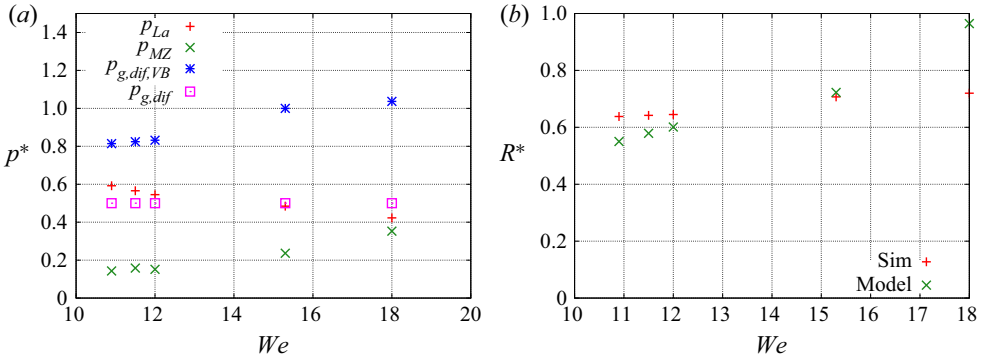

Figure 10. (*a*) Comparison of Laplace pressure (5.14) with liquid inertia (5.15) and gas pressure differences estimated by the VB (5.16) and present (5.17) models as a function of *We* when the rim is formed. (*b*) Comparison of the drop lateral radius when the rim is formed, $\hat{R}^*$, measured from the present simulation and the model prediction (5.18).

The Laplace pressure at the drop periphery at $\hat{t}^*$ can be estimated by assuming that the drop exhibits the shape of a disk:

$$\hat{p}^*_{La} = \frac{\sigma \kappa_N}{\rho_g U_0^2} = \frac{1}{We}\left(12\hat{R}^{*2} + \frac{1}{\hat{R}^*}\right), \tag{5.14}$$

where $\hat{R}^*$ is the dimensionless drop radius for $\hat{t} = \hat{t}^*$. The values of $\hat{p}^*_{La}$ for different *We* are shown in figure 10. Marcotte & Zaleski (2019) suggested that the Laplace pressure when the rim is formed is in equilibrium with the liquid fluid inertia:

$$\hat{p}^*_{MZ} = \frac{\rho_l (\mathrm{d}R/\mathrm{d}t)^2}{\rho_g U_0^2} = \left(\frac{\mathrm{d}\hat{R}}{\mathrm{d}\hat{t}}\right)^2. \tag{5.15}$$

They further proposed to approximate $\mathrm{d}R/\mathrm{d}t$ by the Dimotakis speed, namely $U_0\sqrt{r}$. However, it can be observed in figure 8(*a*) that $U_0\sqrt{r}$ significantly overpredicts $\mathrm{d}\hat{R}/\mathrm{d}\hat{t}$ at $\hat{t}^*$. By using the corrected $(\mathrm{d}\hat{R}/\mathrm{d}\hat{t})$ obtained from simulations, it can be observed from figure 10 that the liquid inertia is significantly lower than $\hat{p}^*_{La}$, thus it is unlikely to be the force that balances the Laplace pressure when the rim is formed.

According to the one-dimensional inviscid model (5.4), when $\mathrm{d}^2\hat{R}/\mathrm{d}\hat{t}^2 = 0$, the liquid pressure at the disk centre and the rim should be in equilibrium, $p_l(0) = p_l(R)$. Since the curvature at the windward pole is approximately zero at this time, $p_l(0) \approx p_g(0)$; see also figure 7(*a*) at $\hat{t} = 0.68$. The liquid pressure at the periphery is $p_l(R) = p_g(R) + p_{La}$. As a result, the Laplace pressure at the rim is actually balanced by the gas pressure difference $\hat{p}_{g,dif} = p_g(0) - p_g(R)$. Villermaux & Bossa (2009) have proposed estimating $p_g(R)$ using the stagnation pressure on the windward surface, namely (5.1):

$$\left(\hat{p}^*_{g,dif}\right)_{VB} = \frac{p_g(0) - p_g(R)}{\rho_g U_0^2} = \frac{a^2\hat{R}^2}{8}, \tag{5.16}$$

where $a = \pi/4$ for a disk. However, the computed pressure field (see figure 7*a*) indicates that the gas pressure above the periphery of the drop, $p_g(R)$, is dictated only by stagnation flow at the windward surface when the drop exhibits an ellipsoidal shape in phase I.

When the drop becomes a disk in phases II and III, the gas flows over the drop periphery without much influence from the windward surface, and as a result, $p_g(R) \approx 0$. Therefore, we estimate the gas pressure difference between the disk centre and periphery as

$$\hat{p}^*_{g,dif} = \frac{p_g(0)}{\rho_g U_0^2} = \frac{1}{2}. \tag{5.17}$$

The results of $(\hat{p}^*_{g,dif})_{VB}$ and $\hat{p}^*_{g,dif}$ are shown in figure 10, and it can be observed that the present estimate $\hat{p}^*_{g,dif}$ agrees better with $\hat{p}^*_{La}$, affirming that the rim formation and the maximal radial expansion velocity before inflation are established when the gas stagnation pressure at the windward pole is in equilibrium with the Laplace pressure at the periphery rim. Furthermore, the pressure balance $\hat{p}^*_{La} = \hat{p}^*_{g,dif}$ yields

$$\frac{1}{We}\left(12{\hat{R}^*}^2 + \frac{1}{\hat{R}^*}\right) = \frac{1}{2}, \tag{5.18}$$

which can be used to predict $\hat{R}^*$ as a function of We for the bag breakup regime. Figure 10(*b*) shows the comparison between the simulation results for $\hat{R}^*$ and the prediction from the model. It can be observed that the increasing trend of $\hat{R}^*$ with We is captured. The agreement between the model predictions and the simulation measurements is generally good for $We = 10.9$ to 15. However, the discrepancy is much larger for $We = 18$, since this case is in the transition to the multi-mode regime.

5.3. *Phase III disk deformation*

After $\mathrm{d}\hat{R}/\mathrm{d}\hat{t}$ reaches a local maximum at the end of phase II, it starts to decrease over time in phase III, when the disk deforms; see figure 7(*d*). The RTI contributes to the subsequent deformation of the windward and leeward surfaces of the disk. As the drop accelerates towards the right, the baroclinic torque induced by the misalignment between the pressure and density gradients destabilizes the windward surface of the disk and stabilizes the leeward counterpart; see $\hat{t} = 0.92$ in figure 7. The deformation of the two surfaces squeezes the liquid to move from the disk centre towards the edge rim (see the distribution of $\hat{u}_y$ in figure 7*b*), resulting in a rapid decrease of disk thickness at the centre h_a and an increase in $\hat{R}$.

There are two mechanisms induced by surface tension that hinder the disk deformation, resulting in the deceleration of the disk edge in the radial direction ($\mathrm{d}^2\hat{R}/\mathrm{d}\hat{t}^2 < 0$). The first mechanism is the surface tension corresponding to the deformation of the windward surface and the resulting curvature on the x–y plane. This surface force is accounted for in the stability analysis of RTI on a flat surface or a planar liquid layer with surface tension (Mikaelian 1990, 1996), which is used to predict the most unstable wavelengths on the windward surface (Joseph *et al.* 1999; Theofanous *et al.* 2004). The second mechanism is the surface force from the rounded edge of the disk. As the radius of curvature is smaller at the lateral edge, a higher pressure develops at the edge, and the resulting pressure gradient resists the disk's lateral expansion, as shown in figure 7 at $\hat{t} = 1.11$. Similar to phases I and II, the second mechanism is the dominant one, and the competition between this mechanism and the Rayleigh–Taylor baroclinic torque seems to determine the drop deformation in this phase.

Though the effect of We can be seen already from $\mathrm{d}\hat{R}/\mathrm{d}\hat{t}$ at the end of phase II, the differences in the drop shapes do not become obvious until phase III; see the temporal

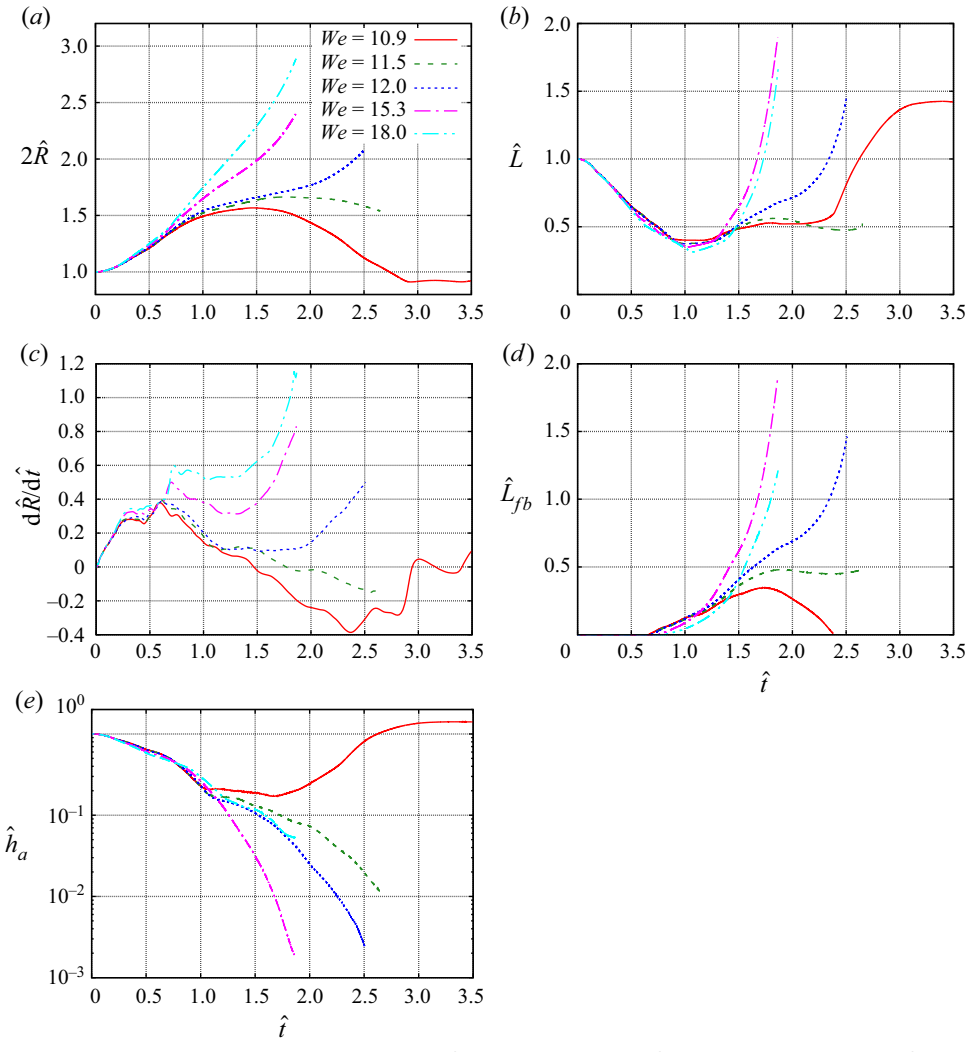

Figure 11. Time evolutions of (*a*) the drop radius $\hat{R}$, (*b*) the drop length $\hat{L}$, (*c*) the rate of change of $\hat{R}$, (*d*) the bag length L_{fb}, and (*e*) the bag sheet thickness along the *x*-axis, for different *We*.

evolutions of the characteristic length scales in figure 11. Phase III is characterized by the decrease of $\mathrm{d}\hat{R}/\mathrm{d}\hat{t}$ in time, and it is observed that phase III starts at approximately $\hat{t} = 0.7$ and ends at approximately $\hat{t} = 1.2$ for all cases except $We = 10.9$.

The evolutions of $\hat{L}_{fb}$ and $\hat{h}_a$ in phase III also showed distinct behaviours; see figure 11. When the drop windward/leeward surfaces become concave, it is hard to measure these two parameters in experiment, but it is easy in the simulation. Due to the definition of $\hat{L}_{fb}$, it remains zero until the windward surface becomes concave in phase III. Though the RTI contributes to the deformation of the windward surface, the growth of $\hat{L}_{fb}$ in the linear regime (when $\hat{L}_{fb}$ is small) is linear instead of exponential. While an exponential growth is expected for the linear RTI on an infinitely flat layer of finite thickness, a possible reason for not observing it here is the surface tension effect at the edge of the disk. The rapid growth of $\hat{L}_{fb}$ for $We = 15.3$ and 18.0 at later times may appear to be exponential, but it

is due to the bag inflation, which will be discussed later, and is not related to the linear stability development. It can be seen that $\hat{h}_a$ decreases monotonically in time, but the rate of decrease in phase III is higher than that in phase II. In addition, kinks are observed in the evolutions of h_a for cases with $We \leq 12$ at approximately $\hat{t} = 1.1$, after which the rate of decrease is significantly reduced. For the case $We = 10.9$, the slow decrease of $\hat{h}_a$ prevents it from reaching the threshold of approximately 0.2 (i.e. the disk thickness remains larger than 20 % of the original drop diameter). As will be shown later, the thick layer at the disk centre hinders the bag growth, and a topology change never happens for this case. It is noteworthy that even a slight increase in We – for instance, from $We = 11.5$ to 12.0 – can cause $\hat{h}_a$ to surpass the critical threshold, leading to the eventual piercing of the bag.

To better illustrate the flow inside the drop and its impact on the drop deformation, the time evolutions of $\hat{u}_y$ inside the drop for different We are also shown in figure 12. It is confirmed that the velocity distributions within the drop for different We are generally similar for phases I and II, and distinctions among different cases arise in phase III. Due to the approximate flow symmetry, $\hat{u}_y$ is close to zero near the centre of the disk ($y = 0$) and is generally positive and negative in the top and bottom portions of the drop in phases I and II for all cases, indicating that the liquid flows outwards from the disk centre. The signs of $\hat{u}_y$ are generally similar in phase III, but the radial flow is not driven by the liquid pressure gradient inside the drop as in phases I and II, but by the RTI on the windward surface. As shown in figure 7(*a*) at $\hat{t} = 1.11$, the pressure actually increases along the radial direction and drives an inward flow back towards the centre, as can be seen in the small regions of $\hat{u}_y < 0$ near the right top corner of the disk for $\hat{t} = 1.04$. For $We = 10.9$ and 11.5, the inward flow gradually overcomes the outward counterpart, as the region for $\hat{u}_y < 0$ in the upper half of the drop grows in time. Eventually, the lateral deformation of the disk changes from expansion to contraction. For $We \leq 12$, the outward flow dominates, and the liquid continues to flow away from the centre, leading to a continuous decrease of h_a, as shown in figure 11.

5.4. *Phase IV: bag development*

The evolution of $\mathrm{d}\hat{R}/\mathrm{d}\hat{t}$ shown in figure 7(*d*) also exhibits a phase for which $\mathrm{d}\hat{R}/\mathrm{d}\hat{t}$ is approximately constant, referred to as phase IV. In this phase, the thin centre of the disk starts to bend towards downstream, forming a forward bag. Here, we define a 'forward bag' as a curved liquid layer with the opening facing upstream. Based on this definition, a 'bag' is formed for all cases; see figure 12. The formation of the bag is due to the baroclinic torque on the unstable windward surface overcoming its counterpart on the stable leeward surface, which in turn is caused by the larger pressure difference on the windward surface. The deformation of the bag enhances liquid flow from the disk centre to the edge, balancing the forces at the edge rim of the disk such that $\mathrm{d}^2\hat{R}/\mathrm{d}\hat{t}^2 = 0$. Phase IV ends when the bag inflates and $\mathrm{d}\hat{R}/\mathrm{d}\hat{t}$ increases rapidly again.

5.4.1. *Criteria for bag piercing*

The evolutions of the characteristic lengths and internal flows for different We are shown in figures 11 and 12. It can be seen that the constant $\mathrm{d}\hat{R}/\mathrm{d}\hat{t}$ is obvious only for $We \leq 12$ and thus is a near-We_{cr} feature. For cases with higher We, the bags start to inflate right after they are formed. Among the three lower We cases considered here, the bag for $We = 10.9$ is stable, the edge of the bag retracts ($\mathrm{d}\hat{R}/\mathrm{d}\hat{t} < 0$), and the thickness of the bag turns to

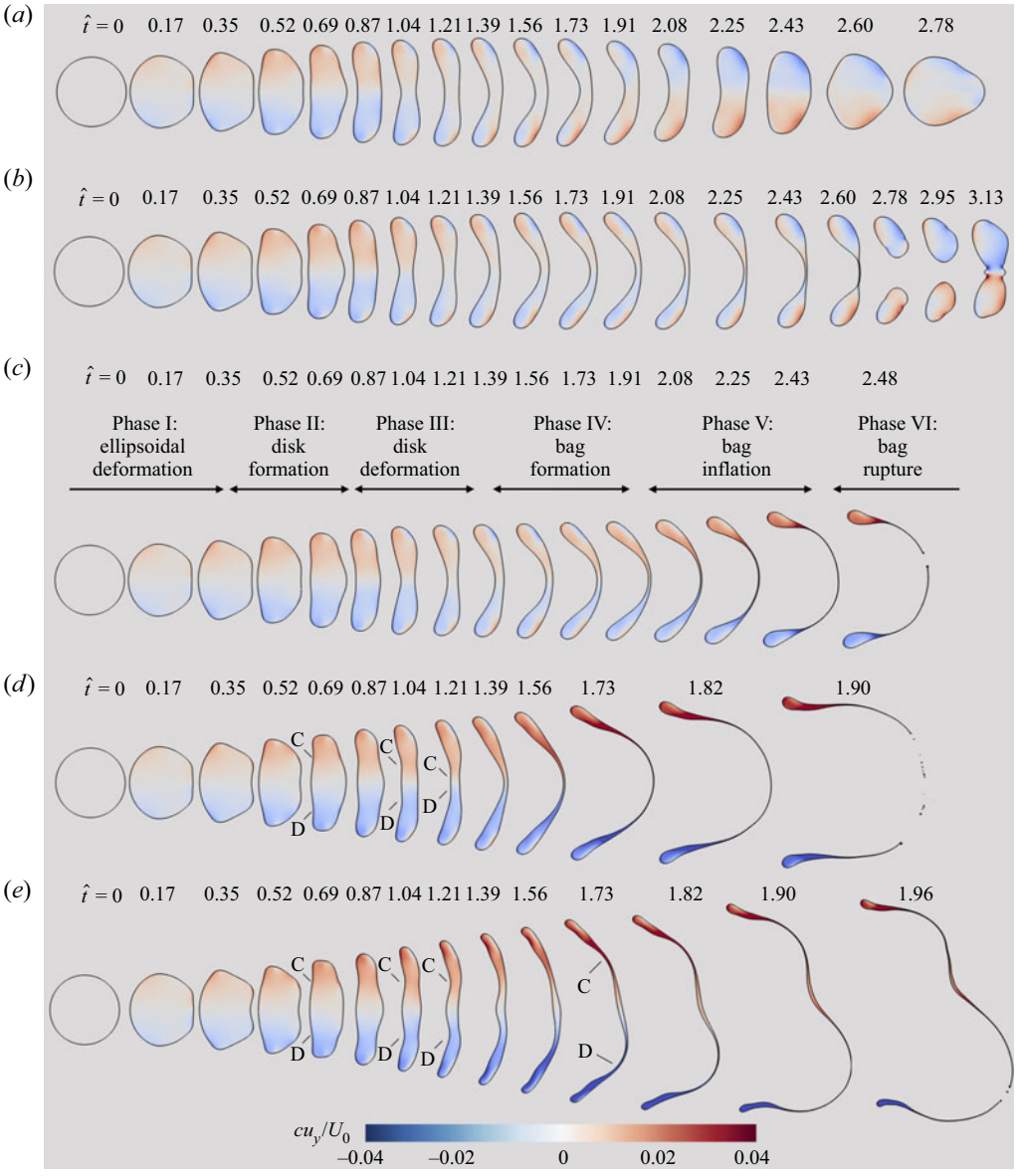

Figure 12. Temporal evolution of the y-velocity (u_y) on the central x–y plane inside the drop for different We values: (*a*) 10.9, (*b*) 11.5, (*c*) 12.0, (*d*) 15.3, and (*e*) 18.0. The points C and D marked in (*d*,*e*) indicate the concave locations on the perturbed windward surface due to drop deformation. Different deformation phases for $We = 12.0$ are indicated in (*c*).

increase in time ($\mathrm{d}\hat{h}_a/\mathrm{d}\hat{t} > 0$). Topology change does not happen (vibration breakup may occur in a long time, but this is outside the scope of this study). In contrast, for $We = 12.0$, the bag is unstable, $\hat{R}$ increases, and $\hat{h}_a$ decreases, and eventually the bag inflates and is pierced through by the gas flow. The results for $We = 11.5$ show an interesting breakup mode that is less understood, i.e. both $\hat{R}$ and $\hat{h}_a$ decrease over time. As a result, the bag will rupture similar to the unstable case $We = 12.0$, but the remaining rim retracts back to form a big drop like the stable case $We = 10.9$. Since the drop for $We = 11.5$ will not

fragment into a large number of small drops, we consider the case $We = 12.0$ to represent the dynamics of aerobreakup at critical conditions, thus $We_{cr} = 12.0$, which is consistent with previous experiments for water drops. Nevertheless, the results for $We = 11.5$ show that bag piercing does not guarantee a complete fragmentation of the bag. The range of We for such behaviour is quite narrow for the density ratios and Reynolds numbers considered, and further investigation of this breakup mode will be relegated to future study.

The linear RTI model with surface tension and viscous effects for an accelerating infinite planar liquid sheet has been proposed to predict the critical condition, such as We_{cr} (Joseph *et al.* 1999; Theofanous *et al.* 2004, 2012), based on the linear stability analysis (Mikaelian 1990, 1996). It was suggested that when the most unstable wavelength is smaller than the disk diameter, a bag will be formed and eventually pierced through by the gas. Although such models, along with other assumptions, capture reasonably the variation of We_{cr} over Oh, the hypotheses of the model are not fully consistent with the flow physics. First, the effect of surface tension at the disk edge was not considered in the model. This simplification is acceptable for perturbations of small wavelengths but not for those with wavelengths comparable to the disk radius R. Furthermore, the previous models predict disk/bag stability based on the linear dynamics of RTI. However, a perturbation that grows in the linear regime (when its amplitude $\hat{L}_{fb}$ is small) does not guarantee its continuous nonlinear growth at later times, and the case $We = 10.9$ explained above is a good example of that.

For cases with $We \leq 15.3$, the forward bag formed is approximately a symmetric spherical shell, and the tip of the bag is located near the central x-axis. Such bags are referred to as 'simple' bags here, and theoretical models have been proposed to predict their formation and development (Villermaux & Bossa 2009; Kulkarni & Sojka 2014). It is considered that the acceleration of the bag tip, which is perpendicular to the free stream, is driven by the pressure difference $(\Delta p)_a$ across the liquid sheet:

$$\frac{\mathrm{d}^2 L_{fb}}{\mathrm{d}t^2} = \frac{(\Delta p)_a}{\rho_l h_a}. \tag{5.19}$$

In this simple model, surface tension and liquid viscosity are ignored. Extensions to incorporate these effects have been made by Kulkarni & Sojka (2014). Since the pressure is hard to measure in experiments, Villermaux & Bossa (2009) approximates the pressure on the leeward side to be the free-stream pressure, and that on the windward side to be the stagnation pressure, so $(\Delta p)_a \approx p_g(r = 0)$, as given in (5.1). For cases with different We, $(\Delta p)_a$ is similar, so the different evolution of L_{fb} is due to mainly the different h_a. The rate of decrease of h_a generally increases with We. As a result, h_a for low We can be significantly larger than that for high We; for example, at $\hat{t} = 1.5$, $h_a = 0.2$ and 0.03 for $We = 10.5$ and 15.3, respectively, and the former is almost an order of magnitude larger than the latter. If h_a is too large, then the tip acceleration is slow compared to the capillary retraction of the edge rim, and h_a will stop decreasing, and the bag will not be pierced through. For the present cases, the evolutions of h_a for $We = 10.5$ and 11.0 bifurcate at $\hat{h}_a = 0.1$–0.2, which seems to indicate that the h_a threshold for bag piercing is approximately 0.2. The value may vary with other parameters that are kept constant in the study, and further investigations are still required to fully confirm this observation.

5.4.2. *Transition from simple to ring bags*

The bag formed for $We = 18.0$ exhibits a more complex shape compared to other cases, as shown in figure 13. First, the bag loses the approximate symmetry observed for $We = 15.3$.

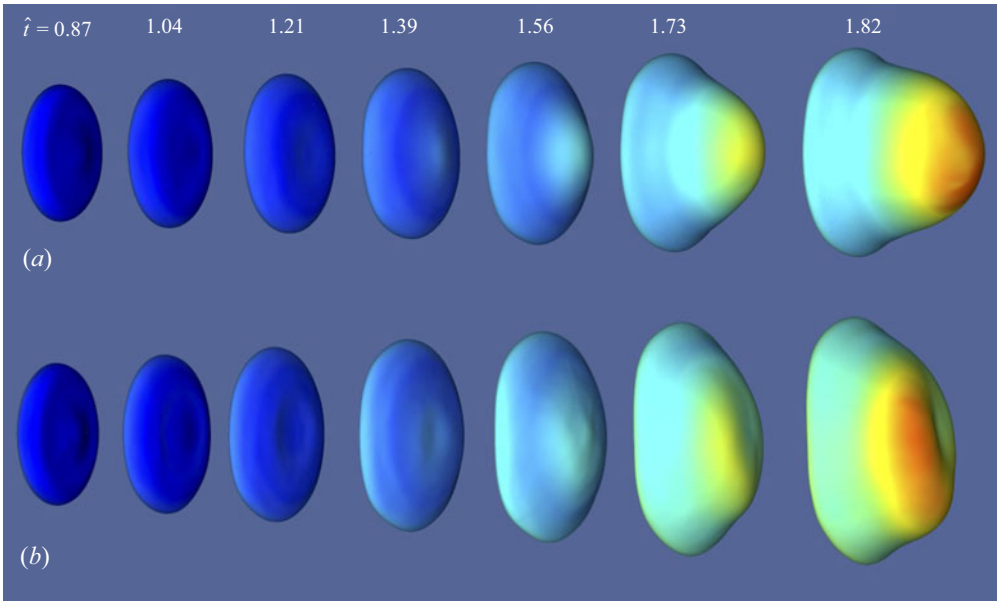

Figure 13. Bag morphological evolutions for (*a*) $We = 15.3$ (simple bag) and (*b*) 18.0 (ring bag). The colour represents the velocity magnitude, and the colour scale is the same as in figure 7.

Furthermore, the minimum thickness of the disk is located not at the bag centre but rather at a ring around it, as seen in figure 12(*e*). As the tip accelerates faster at the location with smaller sheet thickness, the interfacial velocity at $\hat{t} = 1.82$ shown in figure 13(*b*) results in the formation of a 'ring' bag with a dent at the centre. As the ring bag grows, the liquid is squeezed to move away from the tip in two directions. The outward flowing liquid will gather at the rim, and the inward counterpart will gather at the centre to form a small stem, as seen in figure 12(*e*). This drop morphology is also known as the 'bag-stem' mode. As the ring bag grows, transverse RTI may develop and introduce an azimuthal variation of the bag growth rate, leading to the 'multi-bag' mode. A detailed investigation of the bag-stem and multi-bag modes is outside the scope of this paper. However, the present results provide a good understanding of the transition from simple to ring bags and lay the foundation for future studies on the bag-stem and multi-bag modes.

A close look at the drop shapes at $\hat{t} = 0.69$ in figure 12 reveals wavy perturbations formed on the windward surface of the disk. The surface is convex at the centre and concave about $\hat{R}/2$ away from the centre. The concave locations are marked as points C and D in figures 12(*d*) and 12(*e*). The perturbation wavelength is about R, and such a feature holds for all We, making it an outcome of the early-time deformation and independent of We. As the drop for $We = 18.0$ continues to deform, C and D become the locations for the minimum disk thickness where the ring bag is formed. In comparison, for $We \leq 15.3$, C and D merge at the centre, resulting in the minimum thickness being located at the centre. RTI models based on the linear stability of an infinite liquid layer (Theofanous *et al.* 2004) have been used to predict the transition from simple to ring bags. It is argued that the transition will occur when the most unstable Rayleigh–Taylor (RT) wavelength λ_{RT} satisfies $(2R)/\lambda_{RT} = 3$. However, the simulation results presented here suggest a slightly different conclusion. When λ_{RT} is smaller than R, the perturbation on the windward surface will grow and form the ring bag. When $\lambda_{RT} > R$, even if the location of minimum

thickness is initially not at the centre of the bag, it will eventually move back to the centre because the mode with a larger wavelength grows faster.

5.5. *Phase V: bag inflation*

As the thickness of the bag reduces to a certain level, $\hat{h}_a \lesssim 0.02$, the development of the bag enters phase V, as shown in figure 7. For simple bags, the bag in this phase consists of two regions, the rim and the bag sheet, as seen at $\hat{t} = 2.37$ in figure 7. The fraction of the liquid mass in the sheet increases with *We*. The ratios between the masses in the sheet and the rim determine the mass fractions of the child droplets generated by the rupture of the sheet and the rim. In phase V, the sheet portion of the bag inflates. The rapid radial expansion of the sheet also enhances the lateral expansion of the edge rim, resulting in a rapid increase of $\mathrm{d}\hat{R}/\mathrm{d}\hat{t}$, which is the key feature to distinguish phase V from phase IV. This subsection will focus on the inflation of simple bags.

The sheet inflation is driven mainly by the pressure difference across the liquid sheet. It is shown in figure 7(*a*) that $(\Delta p)_a$ varies over time. On the windward side, the gas pressure inside the bag is approximately uniform. The pressure in the bag is initially similar to the stagnation pressure of the free stream. However, as the bag inflates and the bag tip velocity increases, the pressure decreases. On the leeward side, due to flow separation on the lateral edge of the bag, the pressure in the wake is generally lower than the free-stream pressure. Different from the pressure on the windward side of the bag, the pressure on the leeward side increases as the bag inflates due to the resulting delay of flow separation.

The model of Villermaux & Bossa (2009) predicts that the sheet thickness for a disk decays exponentially over time, i.e.

$$\hat{h}_a \sim \exp(-4\hat{t}). \tag{5.20}$$

Then (5.19) can be integrated, yielding two asymptotic limits:

$$\hat{L}_{fb} \sim \hat{t}^2 \quad \text{for } \hat{t} \ll 1, \tag{5.21}$$

$$\hat{L}_{fb} \sim \exp(4\hat{t}) \quad \text{for } \hat{t} \gg 1. \tag{5.22}$$

In the model of Reyssat *et al.* (2007), the bag was approximated as a spherical shell that extends uniformly in all directions. Also assuming that the pressure difference inside and outside scales with the stagnation pressure, they predicted that

$$\hat{L}_{fb} \sim (1 - b\hat{t})^{-2}. \tag{5.23}$$

Then through mass conservation, it can be shown that

$$\hat{h}_a \sim (\hat{L}_{fb})^{-2} \sim (1 - b\hat{t})^4. \tag{5.24}$$

The simulation results for $\hat{h}_a$ for $We = 12.0$ and 15.3 are shown in figure 14(*a*). It can be observed that the early-time decrease of $\hat{h}_a$ in phases I and II is exponential, similar to the model of Villermaux & Bossa (2009). However, since at this time range, the drop is not exactly a disk, the expression for $\hat{h}_a$ should be corrected to

$$\hat{h}_a = \exp(-\hat{t}), \tag{5.25}$$

instead of $\exp(-4\hat{t})$ in the original model. When the bag starts to inflate in the long time, the decay of $\hat{h}_a$ switches to a power law, as predicted by the model of Reyssat *et al.* (2007),

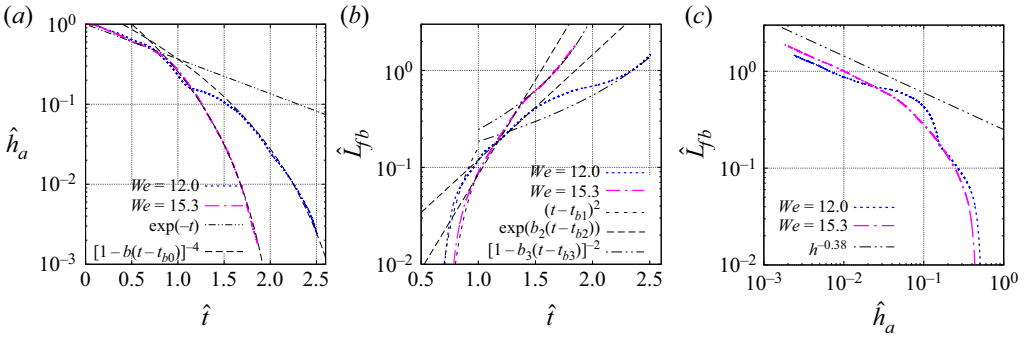

Figure 14. Time evolutions of (*a*) sheet thickness $\hat{h}_a$ and (*b*) bag length $\hat{L}_{fb}$ for the cases $We = 12.0$ and 15.3. (*c*) Plot of $\hat{L}_{fb}$ as a function of $\hat{h}_a$.

i.e.

$$\hat{h}_a = [1 - b(\hat{t} - \hat{t}_{b0})]^{-4}, \tag{5.26}$$

where b and $\hat{t}_{b0}$ are model coefficients that need to be fitted based on the simulation results. In the figure, $b = 0.37$ and 0.58, and $\hat{t}_{b0} = 0.4$ and 0.5, for $We = 12.0$ and 15.3, respectively. The temporal evolutions of $\hat{h}_a$ for $We = 12.0$ and 15.3 are quite similar until the end of phase III ($\hat{t} \approx 1.2$). Afterwards, $\hat{h}_a$ decays faster for $We = 15.3$, which is due to mainly the long phase IV for $We = 12.0$, during which $\hat{h}_a$ decays more gradually.

The evolution of $\hat{L}_{fb}$ is shown in figure 14(*b*). In the early time of bag inflation, $\hat{L}_{fb}$ increases with time following a power law, similar to (5.21). We have to add a case-dependent parameter $\hat{t}_{b1}$, i.e.

$$\hat{L}_{fb} = (\hat{t} - \hat{t}_{b1})^2, \tag{5.27}$$

where the fitted values for $\hat{t}_{b1}$ are 0.6 and 0.7 for $We = 12.0$ and 15.3, respectively. In the intermediate term, when the drop deforms as a disk, the increase of $\hat{L}_{fb}$ is exponential, as predicted by the model of Villermaux & Bossa (2009) and (5.22). It is found that

$$\hat{L}_{fb} = \exp[b_2(\hat{t} - \hat{t}_{b2})], \tag{5.28}$$

where $b_2 = 2.5$ and 4.5, and $\hat{t}_{b2} = 1.85$ and 1.55, for $We = 12.0$ and 15.3, respectively. Similar trends have also been observed in the experiments (Villermaux & Bossa 2009). In the long time, when the bag inflates and deforms as a shell with decreasing thickness, it is observed that $\hat{L}_{fb}$ increases following another power law, similar to (5.23) given by the model of Reyssat *et al.* (2007), i.e.

$$\hat{L}_{fb} = [1 - b_3(\hat{t} - \hat{t}_{b3})]^{-2}, \tag{5.29}$$

where $b_3 = 0.98$ and 1.5, and $\hat{t}_{b3} = 2.35$ and 1.68, for $We = 12.0$ and 15.3, respectively. During bag inflation, $\hat{L}_{fb}$ increases with decreasing $\hat{h}_a$; see figure 14(*c*). The variation of $\hat{L}_{fb}$ for small $\hat{h}_a$ follows a power law, yet the power index is -0.38, instead of -0.5 given by (5.24). The agreement between the present simulation results with the theoretical scaling relations indicates that the early stage of bag inflation is well captured.

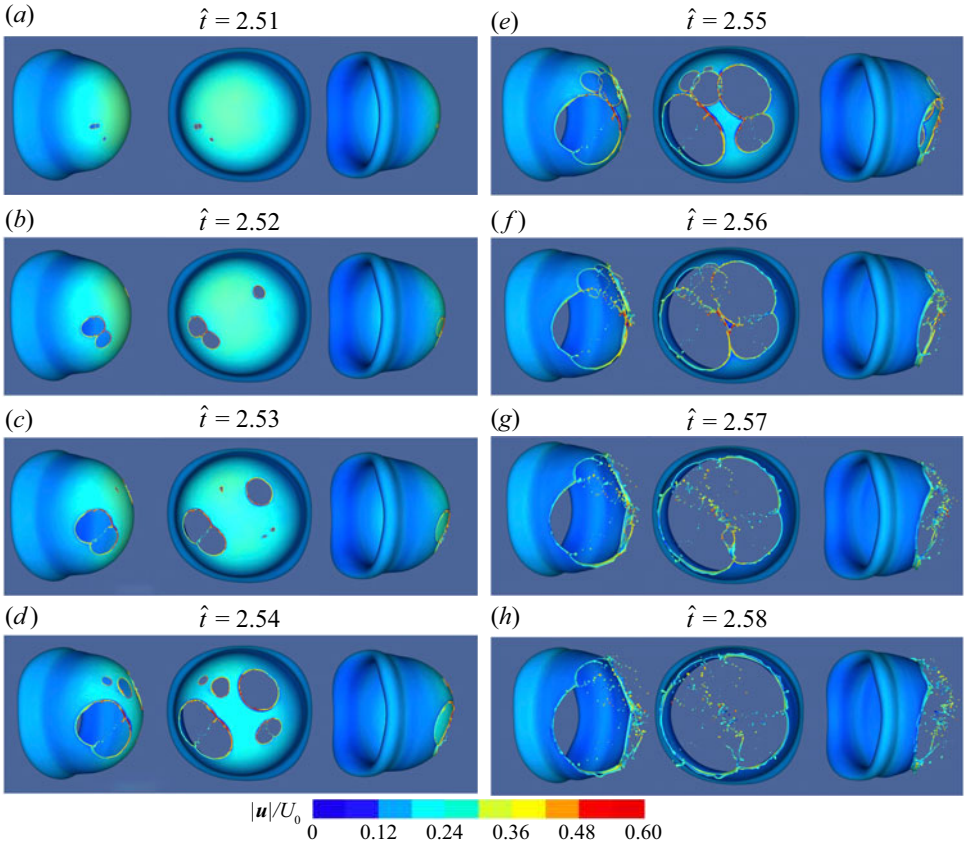

Figure 15. Time evolution of the drop surface from $\hat{t} = t/\tau_d = 2.51$ to 2.58 for $We = 12.0$, showing the breakup of the bag due to appearance and merging of holes. The colour on the interfaces represents the velocity magnitude. The three different views are shown for each time.

5.6. *Phase VI bag rupture*

As the bag sheet thickness continues to decrease, the two interfaces will eventually pinch, forming a hole in the liquid sheet. Generally, holes are formed at different locations at different times. The holes will expand as the rim retracts with the Taylor–Culick velocity (Opfer *et al.* 2014; Ling *et al.* 2017; Agbaglah 2021). When different holes merge, the liquid sheet rupture completely, producing numerous small filaments and droplets, and the remaining rim. The bag rupture process for $We = 12.0$ is shown in figure 15.

5.6.1. *Effect of numerical breakup*

In an ideal scenario without any tiny bubbles or contaminants in the liquid sheet and with no thermal fluctuations, as considered in the present simulations, the two interfaces will eventually pinch, resulting in holes in the liquid sheet. Van der Waals forces become important to the interfacial dynamics when the sheet thickness is between approximately 10 and 100 nm, and the interactions between van der Waals forces and surface tension typically dictate the sheet rupture and hole formation. The critical sheet thickness at which holes first appear due to van der Waals forces is referred to as the physical cutoff length, which is of the order of tens of nanometres. While the rupture dynamics of a stationary free

liquid sheet has been studied extensively (Erneux & Davis 1993; Ida & Miksis 1996), the rupture of a dynamic moving sheet is less understood, and the corresponding critical sheet thickness could be significantly larger, as indicated in the drop aerobreakup experiment by Opfer *et al.* (2014). The minimum cell size in a 3-D simulation, referred to as the numerical cutoff length, is significantly larger than the physical counterpart, and therefore the interface pinching occurs earlier in the simulation. When the liquid sheet thickness reduces to approximately twice the minimum cell size of the octree mesh, numerical error in VOF reconstruction will act as a perturbation on the interfaces, which eventually causes numerical pinching between the two interfaces of the sheet. The interface pinching will form small holes in the liquid sheet. The numerical breakup of the VOF method has both pros and cons. On one hand, it will allow topology change automatically, and no additional procedure is required as needed for other methods like the front-tracking method (Lu & Tryggvason 2018). On the other hand, the length scale for pinching to occur is related to mesh resolution. As a result, it will not produce mesh-independent results for liquid sheet breakup and hole formation. Recently, the manifold death method has been proposed by Chirco *et al.* (2022) to model sheet rupture. Thin sheets are detected by taking quadratic moments of an indicator obtained from the VOF function, then pinching is induced manually based on a user-defined cutoff length that is independent of the cell size. The manifold death method has been applied recently to simulate bag breakup by Chirco *et al.* (2022) and Tang *et al.* (2023), and it was observed that the method reduces the influence of numerical breakup on hole formation. Nevertheless, since the cutoff length scale in the manifold death method needs to be larger than the cell size, it will not produce 'more physical' results unless the mesh resolution is comparable to the physical length scale. The larger numerical cutoff length, which is approximately 1 μm in the present simulation, will cause hole formation earlier than in reality, and as a result, the numerical simulation will not be able to capture the late stage of bag inflation and the bag rupture.

In spite of the limitations of the numerical simulation, the results at different resolutions obtained here are still useful for understanding the bag rupture dynamics, and the results can be used to extrapolate the unresolved stage of bag inflation. The evolution of the total surface area of the drop, normalized by its initial value, i.e. S/S_0, for $We = 12.0$, is shown in figure 16(a). During the interaction between the drop and the free stream, the gas kinetic energy is transferred to the surface energy of the drop, thus the surface area increases over time. After holes are formed, the surface area will change to decrease due to the capillary expansion of the holes. Therefore, S reaches the maximum value at approximately the onset time for sheet breakup. As the mesh resolution increases from $N = 512$ to 2048, the breakup is delayed, and we can resolve the bag until $S/S_0 \approx 5.5$ with $N = 2048$. According to figure 14(a) and the fitted function (5.26), one can estimate the breakup time for a given physical cutoff length smaller than the minimum cell size. Then, based on the estimated breakup time, extrapolation from figure 16(a) can be used to estimate the surface area when the bag breaks according to the physical cutoff length.

The bag morphology when holes are just formed is shown in figures 16(b), 16(c), and 16(d) for $N = 512$, 1024 and 2048, respectively. Typically, the holes formed due to the lack of resolution in VOF reconstruction exhibit irregular shapes. Yet after they are formed, surface tension tends to regularize the shape of the hole and to form a rim on the edge of the hole. For $N = 512$, many small holes are formed simultaneously, thus holes start to interact with each other before the rim gets a chance to develop. With the most refined mesh, $N = 2048$, only three small holes are formed initially, and the subsequent evolutions of rims and holes are well captured; see also figure 15.

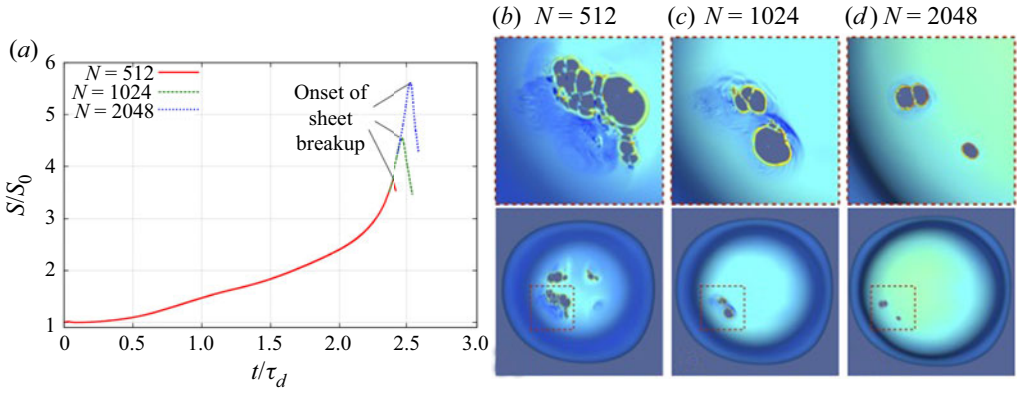

Figure 16. Effect of mesh resolution on the bag bursting for $We = 12.0$. (*a*) Time evolution of the drop surface area. (*b–d*) Drop surfaces when the holes are just formed for different mesh resolutions $N = 512$, 1024, 2048, respectively.

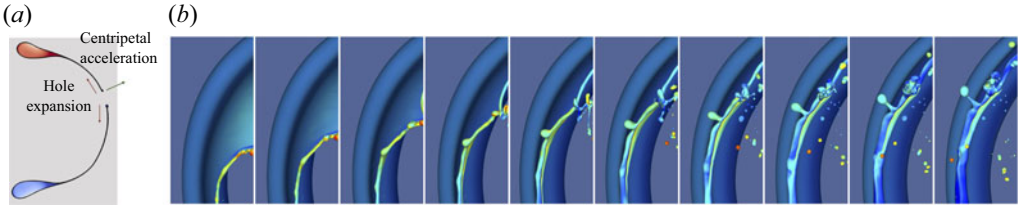

Figure 17. The RTI due to centripetal acceleration of the rim, forming fingers at the rim, which later detach to form child droplets. The results are for $We = 12.0$ and $\hat{t} = 2.534$–2.589, with increment 0.008. The colour on the interfaces represents the velocity magnitude; see figure 15 for the colour scale.

5.6.2. *Hole dynamics and drop formation*

After a hole is formed, the capillary retraction of the rim causes the hole to expand. The rim retraction velocity is the Taylor–Culick velocity $U_{TC} = \sqrt{2\sigma/\rho_l h}$, where h is the sheet thickness near the rim. As the sheet thickness in the bag is quite uniform, the rim retraction velocity is approximately constant and agrees well with U_{TC} (Ling *et al.* 2017; Agbaglah 2021). Nevertheless, as the rim moves along the curved liquid sheet, it experiences a centripetal acceleration along the radial direction of the bag; see figure 17(*a*). Along with the density difference, an RTI is triggered along the rim. The development of RTI leads to the formation of fingers normal to the rim pointing outwards. The subsequent Rayleigh–Plateau instability of the fingers detaches droplets. The process of finger formation and drop detachment at the rim is shown in figure 17(*b*). The colour on the interface represents the velocity magnitude, from which the interfacial velocity variation along the rim can be recognized. Similar drop formation processes were also observed in bubble bursting (Lhuissier & Villermaux 2012).

Figure 18 shows the interaction between two holes. It can be observed that when the rims of different holes collide, a new fish-shaped liquid lamella is formed, the disintegration of which produces a large number of small droplets. The hole–hole interaction has been investigated recently by Agbaglah (2021) and Tang *et al.* (2023) through numerical simulation. The simulation results of Agbaglah (2021) show that the collision of rims forms a rim instead of a lamella as observed here and in the results of Tang *et al.* (2023). The discrepancy is probably due to the fact that the sheet thicknesses considered by

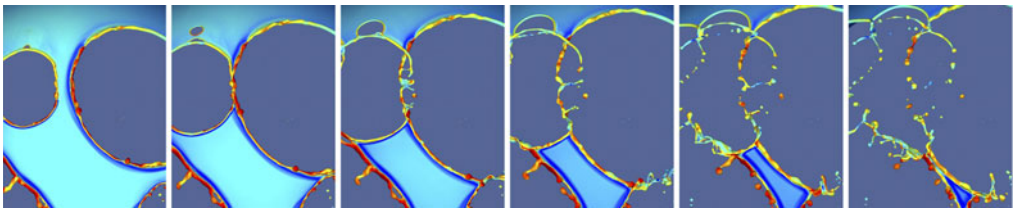

Figure 18. Interactions between rims of different holes when the hole-merging occurs. The results are for $We = 12.0$ and $\hat{t} = t/\tau_d = 2.544$–$2.562$ with increment 0.004. The colour on the interfaces represents the velocity magnitude; see figure 15 for the colour scale.

Agbaglah (2021) are larger than those in the present cases. The small sheet thickness leads to a higher rim retraction velocity when they collide. This is also why the lamella formation was not observed in the present simulations with coarser meshes. Neel, Lhuissier & Villermaux (2020) suggested characterizing the rim collision dynamics using the Weber number We_h, defined based on U_{TC} and rim radius. It can be shown that We_h is proportional to the ratio between the holes' distance and the sheet thickness. When We_h is sufficiently large, the rim collision will generate an expanding lamella with transverse modulation on the rim. The lamella will also break later to form a distribution of child droplets.

While the present simulations are useful in revealing the qualitative droplet formation mechanisms, the larger numerical cutoff length scale will not allow for a quantitative prediction of the statistics of the droplets formed from the bag rupture. Such a prediction will be possible only if one can use a mesh resolution down to the physical cutoff length, or if a subgrid sheet model can be developed to represent the unresolved sheet inflation and breakup dynamics. These tasks are relegated to future works.

6. Turbulent wake and drop dynamics

6.1. *Effect of drop deformation on the aerodynamic drag and lift*

In the aerobreakup process, the drop accelerates due to aerodynamic drag. As discussed in § 3.3, the unsteady contributions to the drag, triggered by the impulsive gas acceleration, to the drop velocity are generally small due to the low gas-to-liquid density ratio. The drop acceleration is dictated mainly by the quasi-steady drag corresponding to the relative velocity $U_0 - u_d$. The shape deformation has a strong impact on the quasi-steady drag and the resulting drop acceleration. The temporal evolutions of the normalized drop velocity $\hat{u}_d$, for different We, are shown in figure 19(a). When We increases, the drop deforms more significantly, and the drop velocity increases faster. It can be seen that the drop velocity reaches approximately 18 % of U_0 for $We = 18.0$ when the drop breaks, compared to approximately 12 % for $We = 15.3$.

The lateral radius R is the characteristic length for the gas flow around the drop, based on which the instantaneous drop Reynolds number is defined as

$$Re_d = \frac{\rho_g (U_0 - u_d) 2R}{\mu_g}. \tag{6.1}$$

The evolutions of Re_d for different We are shown in figure 19(b). At time zero, $Re_d = Re$. As time evolves, the differences in Re_d for different cases are magnified. Though the relative velocity $U_0 - u_d$ decreases over time, Re_d increases, thanks to the rapid increase of R. For $We = 18.0$, Re_d can increase to almost three times its initial value. For the cases $We = 10.9$ and 11.5, when $\hat{R}$ turns to decrease at later time, Re_d also decreases. For all the

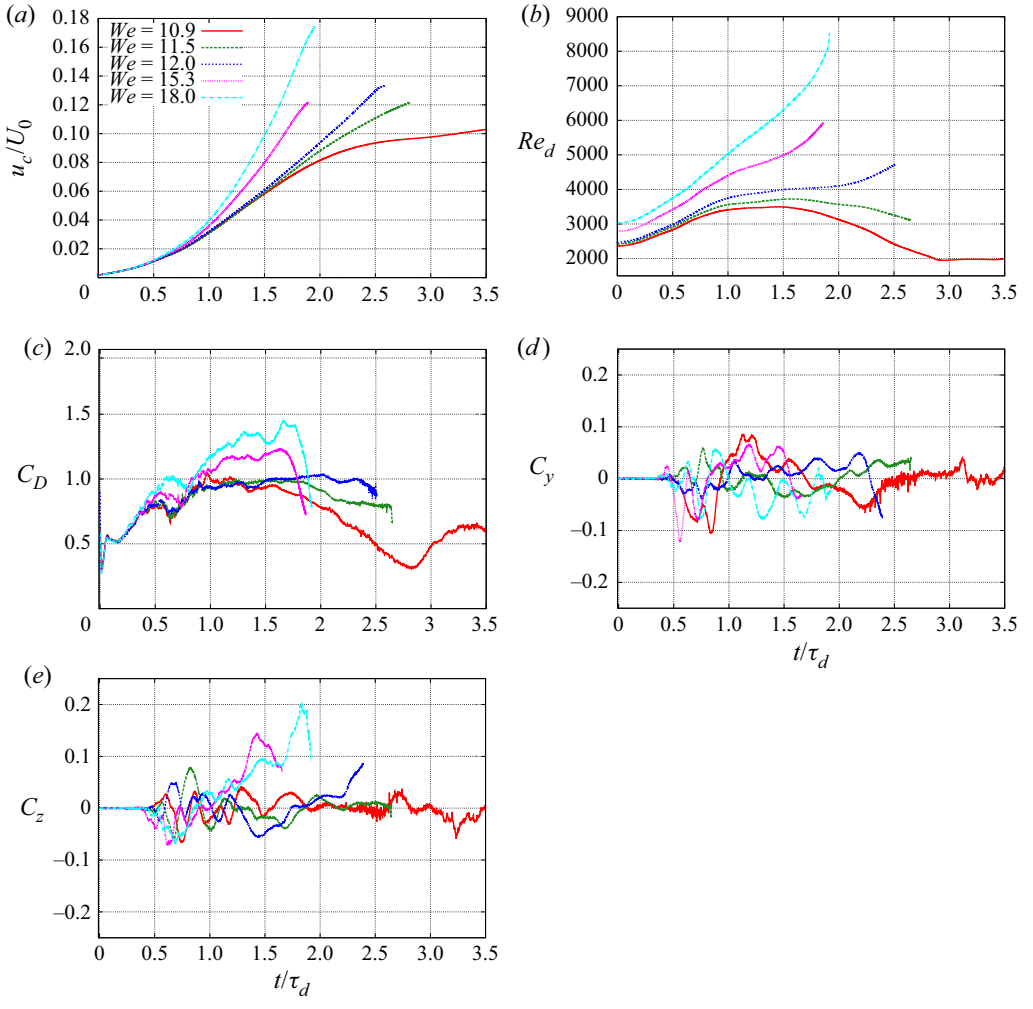

Figure 19. Time evolutions of (*a*) streamwise velocity of the drop u_c, (*b*) drop Reynolds number Re_d, (*c*) drag coefficient C_D, and (*d*,*e*) lift coefficients in the lateral *y*- and *z*-directions, for drops at different *We*.

cases considered, Re_d varies between approximately 2000 and 8000. For a solid sphere, this range of Re_d lies in the chaotic vortex shedding regime and subcritical turbulent wake regime (Tiwari *et al.* 2020*a*). The shedding of the turbulent wake can be observed in figure 6(*c*).

Since the drag coefficient C_D is defined (see (3.3)) based on the instantaneous relative velocity and drop radius, the time variations of $U_0 - u_d$ and R actually do not contribute to changes in C_D over time. While a constant C_D is often assumed in previous studies (Marcotte & Zaleski 2019), a non-monotonic time evolution of C_D is observed here, as shown in figure 19(*c*), which is due to the complex drop shape deformation in different phases. Once again, we take the case $We = 12.0$ as the representative example to explain the physics behind it. When the drop remains approximately a sphere at early time, $C_D \approx 0.5$, which is expected for a spherical drop with large density and viscosity contrast. Then, as the drop deforms into an ellipsoid with decreasing streamwise thickness in phase I, C_D increases until it reaches a local maximum. When the drop continues to deform into a disk

in phase II, C_D increases again until it reaches a plateau value of approximately 1, which is similar to the typical C_D for a thin, flat circular disk. When the disk deforms into a bag in phases III and IV due to RTI, the change in the drop shape is relatively small, so C_D increases slowly. When the bag inflates in phase V, as the bag shape becomes more aligned with the gas flow, C_D decreases. The amplitude of variation in C_D is generally more profound for cases with larger *We*.

6.2. *Effect of transient development of gas flow*

The present configuration involves a sudden exposure of the drop to the free stream, which causes the boundary layer around the drop to take a finite time to develop, as shown in figure 6(*c*). This boundary layer development contributes to viscous-unsteady drag and the resulting large amplitude variation of C_D near $\hat{t} = 0$. Despite the high Reynolds numbers, the flow remains approximately axisymmetric in phase I, and the transition to a turbulent wake does not occur until phase II. The formation of the disk in phase II enhances flow separation and accelerates the transition of the wake to turbulence. When the wake becomes turbulent, the gas pressure on the leeward side of the drop increases, as shown at $\hat{t} = 0.79$ in figure 6(*b*). Consequently, the drag decreases at $\hat{t} \approx 0.6$–0.7, as shown in figure 19(*c*). The breakdown of wake symmetry induces lift on the drop. The lift coefficients in the lateral y- and z-directions are initially zero since the flow around the drop is approximately axisymmetric, but C_y and C_z become non-zero and start to oscillate in time approximately $\hat{t} = 0.4$, as shown in figures 19(*d*) and 19(*e*). The low-frequency oscillation observed in the lift coefficients is related to the shedding of the wake. The wake features are consistent with the range of *Re* for the present cases.

7. Conclusions

Detailed numerical simulations were performed in the present study to investigate the drop aerobreakup in the moderate Weber number (*We*) regime. We have considered an ideal configuration, in which an initially stationary and spherical drop is subjected to a uniform gas stream. The liquid and gas are taken to be water and air, and the drop size is fixed at 1.9 mm, following the experiment of Jackiw & Ashgriz (2021). A parametric study is carried out by varying the gas stream velocity (U_0). Due to the interaction with the uniform gas stream, the drop deforms from a sphere to a forward bag with the opening facing upstream. When *We* is sufficiently high, the bag is unstable and will eventually inflate and be pierced through by the gas stream.

The numerical simulations were performed using the Basilisk solver. The mass–momentum consistent volume-of-fluid method is used to captured the sharp gas–liquid interface. The computational domain is discretized using quadtree/octree mesh, and an adaptive mesh refinement technique is employed to reduce the total number of cells. To resolve the bag inflation and rupture dynamics, the finest mesh used in the simulation is equivalent to 2048 cells across the initial drop diameter.

The key findings of the present study are summarized as follows.

(i) High-resolution 3-D simulation is necessary to capture drop aerobreakup. Both 2-D axisymmetric and 3-D simulations were performed, using identical numerical methods and initial/boundary conditions. The converged 2-D simulation results are shown to be significantly different from the 3-D simulation and experimental results, because 2-D simulations cannot resolve the turbulent wake, and as a result, will not be able to capture the correct bag shape and drop acceleration. Grid-refinement

studies were performed for the 3-D simulations, and the adaptive mesh with a minimum cell size equivalent to 512 cells across the initial drop diameter is sufficient to yield mesh-independent results for the drop shape, drag coefficient and gas enstrophy. The 3-D simulation results are compared against previous experiments, and good agreement is achieved.

(ii) Different phases in the drop morphological evolution are identified. The non-monotonic evolution of the rate of change of the lateral drop radius ($\mathrm{d}R/\mathrm{d}t$) shows clearly different phases in the overall process, including (I) ellipsoid deformation, (II) disk formation, (III) disk deformation, (IV) bag development, (V) bag inflation, and (VI) bag rupture.

(iii) The asymptotic early-time drop dynamics is independent of We. In the asymptotic limit of $t \to 0$, the evolutions of the drop shapes for different We collapse. This We independence in early-time drop dynamics is consistent with the time scale analysis and is affirmed further by the good agreement between drop velocities obtained by the present simulations and the inviscid compressible simulations in previous studies.

(iv) A new internal-flow deformation model is proposed for phase I. The drop deforms as an ellipsoid in phase I, and the deformation is dictated by the internal flow, which is, in turn, driven by the stagnation flow near the windward pole. An improved internal-flow deformation model is proposed, which respects the We-independent asymptotic limit at time zero. The results of the present model show better agreement with the present simulation results, compared to previous models.

(v) The disk is formed when the Laplace pressure at the edge is in balance with the stagnation pressure. The drop deforms towards a disk with a rounded edge in phase II. The edge rim of the disk is formed when $\mathrm{d}R/\mathrm{d}t$ reaches a local maximum, namely $\mathrm{d}^2R/\mathrm{d}t^2 = 0$, and the Laplace pressure at the edge rim reaches a balance with the gas stagnation pressure on the windward surface.

(vi) The RTI dictates the thinning of the disk centre. When the disk is accelerated along the streamwise direction, the windward surface is unstable while the leeward surface is stable. The development of the RTI becomes the dominant mechanism for the continuous drop lateral extension and the thinning of the disk centre in phase III. The surface tension at the edge rim resists the RTI development, and as a result, $\mathrm{d}R/\mathrm{d}t$ decreases in time.

(vii) Bag piercing does not guarantee bag fragmentation. When the thin disk centre curves downstream, the disk deforms to a forward bag. The bag can be pierced through by the gas stream only if the minimum thickness of the disk can decrease to be lower than a threshold, which is approximately 20 % of the original drop diameter. More importantly, when We is just lower than We_{cr}, the bag can be pierced through but does not fragment into droplets, as the ring rim will retract towards the centre and eventually will turn back to a big drop.

(viii) Evolutions of the bag length and sheet thickness follow similar power laws when the bag inflates. In phase V, the rapid inflation of the bag causes the rim lateral velocity $\mathrm{d}R/\mathrm{d}t$ to increase rapidly over time. The increase of the bag length and the decrease of the sheet thickness follow exponential functions initially and then switch to power laws. The agreement with the power-law scaling actually indicates that the sheet expands uniformly in all directions when the bag inflates. That is because the gas pressure is approximately uniform inside the bag.

(ix) Hole–hole interaction is important to the disintegration of the bag. The numerical cutoff length is significantly larger than the physical counterpart, thus the bags in the

simulations break earlier than in reality. Nevertheless, the simulation results for the most refined mesh well capture the dynamics of holes. When two holes merge, the collision between the two rims forms a lamella first, then the lamella disintegrates into small droplets.

(x) The drop morphological change has a strong impact on the drag coefficient. The evolutions of the drop deformation and acceleration are coupled closely. Due to the low gas-to-liquid density ratio, the drop acceleration is due mainly to the quasi-steady drag. Although the relative velocity $U_0 - u_d$ decreases in time, the instantaneous Reynolds number increases with R. The non-monotonic evolution of the drag coefficient C_D is caused mainly by the change of drop shape; C_D decreases over time as the bag inflates, and the flow separation is delayed.

Supplementary material. Supplementary movies are available at https://doi.org/10.1017/jfm.2023.708.

Acknowledgements. The XSEDE/ACCESS and Frontera programmes have provided the computational resources that contributed to the simulation results reported in this paper. The Baylor High Performance and Research Computing Services (HPRCS) have been used for the simulation and data processing. The authors would also like to acknowledge S. Zaleski, N. Rimbert, J. McFarland and F. Marcotte for helpful discussions. The present simulations were performed using the Basilisk solver, which is made available by S. Popinet and other collaborators.

Funding. This research is supported by the ACS Petroleum Research Fund (no. 62481-ND9) and the NSF (no. 1942324).

Declaration of interests. The authors report no conflict of interest.

Author ORCIDs.
Y. Ling https://orcid.org/0000-0002-0601-0272.

References

Agbaglah, G.G. 2021 Breakup of thin liquid sheets through hole–hole and hole–rim merging. *J. Fluid Mech.* **911**, A23.

Apte, S.V., Gorokhovski, M. & Moin, P. 2003 LES of atomizing spray with stochastic modeling of secondary breakup. *Intl J. Multiphase Flow* **29**, 1503–1522.

Arrufat, T., Crialesi-Esposito, M., Fuster, D., Ling, Y., Malan, L., Pal, S., Scardovelli, R., Tryggvason, G. & Zaleski, S. 2020 A momentum-conserving, consistent, volume-of-fluid method for incompressible flow on staggered grids. *Comput. Fluids* **215**, 104785.

Balachandar, S. 2009 A scaling analysis for point particle approaches to turbulent multiphase flows. *Intl J. Multiphase Flow* **35**, 801–810.

Blanco, A. & Magnaudet, J. 1995 The structure of the axisymmetric high-Reynolds number flow around an ellipsoidal bubble of fixed shape. *Phys. Fluids* **7**, 1265–1274.

Burelbach, J.P., Bankoff, S.G. & Davis, S.H. 1988 Nonlinear stability of evaporating/condensing liquid films. *J. Fluid Mech.* **195**, 463–494.

Chang, C.-H., Deng, X. & Theofanous, T.G. 2013 Direct numerical simulation of interfacial instabilities: a consistent, conservative, all-speed, sharp-interface method. *J. Comput. Phys.* **242**, 946–990.

Chirco, L., Maarek, J., Popinet, S. & Zaleski, S. 2022 Manifold death: a volume of fluid implementation of controlled topological changes in thin sheets by the signature method. *J. Comput. Phys.* **467**, 111468.

Chou, W.-H. & Faeth, G.M. 1998 Temporal properties of secondary drop breakup in the bag breakup regime. *Intl J. Multiphase Flow* **24**, 889–912.

Dai, Z. & Faeth, G.M. 2001 Temporal properties of secondary drop breakup in the multimode breakup regime. *Intl J. Multiphase Flow* **27**, 217–236.

Erneux, T. & Davis, S.H. 1993 Nonlinear rupture of free films. *Phys. Fluids* A **5**, 1117–1122.

Flock, A.K., Guildenbecher, D.R., Chen, J., Sojka, P.E. & Bauer, H.-J. 2012 Experimental statistics of droplet trajectory and air flow during aerodynamic fragmentation of liquid drops. *Intl J. Multiphase Flow* **47**, 37–49.

GAO, J., GUILDENBECHER, D.R., REU, P.L., KULKARNI, V., SOJKA, P.E. & CHEN, J. 2013 Quantitative, three-dimensional diagnostics of multiphase drop fragmentation via digital in-line holography. *Opt. Lett.* **38**, 1893–1895.

GUILDENBECHER, D.R., GAO, J., CHEN, J. & SOJKA, P.E. 2017 Characterization of drop aerodynamic fragmentation in the bag and sheet-thinning regimes by crossed-beam, two-view, digital in-line holography. *Intl J. Multiphase Flow* **94**, 107–122.

GUILDENBECHER, D.R., LÓPEZ-RIVERA, C. & SOJKA, P.E. 2009 Secondary atomization. *Exp. Fluids* **46**, 371.

HADJ-ACHOUR, M., RIMBERT, N., GRADECK, M. & MEIGNEN, R. 2021 Fragmentation of a liquid metal droplet falling in a water pool. *Phys. Fluids* **33**, 103315.

HAN, J. & TRYGGVASON, G. 1999 Secondary breakup of axisymmetric liquid drops. I. Acceleration by a constant body force. *Phys. Fluids* **11**, 3650–3667.

HAN, J. & TRYGGVASON, G. 2001 Secondary breakup of axisymmetric liquid drops. II. Impulsive acceleration. *Phys. Fluids* **13**, 1554–1565.

HARPER, E.Y., GRUBE, G.W. & CHANG, I.-D. 1972 On the breakup of accelerating liquid drops. *J. Fluid Mech.* **52**, 565–591.

HINZE, J.O. 1955 Fundamentals of the hydrodynamic mechanism of splitting in dispersion processes. *AIChE J.* **1**, 289–295.

VAN HOOFT, J.A., POPINET, S., VAN HEERWAARDEN, C.C., VAN DER LINDEN, S.J.A., DE ROODE, S.R. & VAN DE WIEL, B.J.H. 2018 Towards adaptive grids for atmospheric boundary-layer simulations. *Boundary-Layer Meteorol.* **167**, 421–443.

HSIANG, L.-P. & FAETH, G.M. 1992 Near-limit drop deformation and secondary breakup. *Intl J. Multiphase Flow* **18**, 635–652.

HSIANG, L.-P. & FAETH, G.M. 1995 Drop deformation and breakup due to shock wave and steady disturbances. *Intl J. Multiphase Flow* **21**, 545–560.

IDA, M.P. & MIKSIS, M.J. 1996 Thin film rupture. *Appl. Maths Lett.* **9**, 35–40.

JACKIW, I.M. & ASHGRIZ, N. 2021 On aerodynamic droplet breakup. *J. Fluid Mech.* **913**, A33.

JACKIW, I.M. & ASHGRIZ, N. 2022 Prediction of the droplet size distribution in aerodynamic droplet breakup. *J. Fluid Mech.* **940**, A17.

JAIN, M., PRAKASH, R.S., TOMAR, G. & RAVIKRISHNA, R.V. 2015 Secondary breakup of a drop at moderate Weber numbers. *Proc. R. Soc. Lond.* A **471**, 20140930.

JAIN, S.S., TYAGI, N., PRAKASH, R.S., RAVIKRISHNA, R.V. & TOMAR, G. 2019 Secondary breakup of drops at moderate Weber numbers: effect of density ratio and Reynolds number. *Intl J. Multiphase Flow* **117**, 25–41.

JALAAL, M. & MEHRAVARAN, K. 2014 Transient growth of droplet instabilities in a stream. *Phys. Fluids* **26**, 012101.

JING, L. & XU, X. 2010 Direct numerical simulation of secondary breakup of liquid drops. *Chinese J. Aeronaut.* **23**, 153–161.

JOSEPH, D.D., BELANGER, J. & BEAVERS, G.S. 1999 Breakup of a liquid drop suddenly exposed to a high-speed airstream. *Intl J. Multiphase Flow* **25**, 1263–1303.

KEKESI, T., AMBERG, G. & WITTBERG, L.P. 2014 Drop deformation and breakup. *Intl J. Multiphase Flow* **66**, 1–10.

KULKARNI, V. & SOJKA, P.E. 2014 Bag breakup of low viscosity drops in the presence of a continuous air jet. *Phys. Fluids* **26**, 072103.

LEE, C.S. & REITZ, R.D. 2001 Effect of liquid properties on the breakup mechanism of high-speed liquid drops. *Atomiz. Spray* **11**, 1–19.

LHUISSIER, H. & VILLERMAUX, E. 2012 Bursting bubble aerosols. *J. Fluid Mech.* **696**, 5–44.

LING, Y., FUSTER, D., ZALESKI, S. & TRYGGVASON, G. 2017 Spray formation in a quasiplanar gas–liquid mixing layer at moderate density ratios: a numerical closeup. *Phys. Rev. Fluids* **2**, 014005.

LING, Y., HASELBACHER, A. & BALACHANDAR, S. 2011 Importance of unsteady contributions to force and heating for particles in compressible flows. Part 1: modeling and analysis for shock–particle interaction. *Intl J. Multiphase Flow* **37**, 1026–1044.

LING, Y., PARMAR, M. & BALACHANDAR, S. 2013 A scaling analysis of added-mass and history forces and their coupling in dispersed multiphase flows. *Intl J. Multiphase Flow* **57**, 102–114.

LIU, A.B. & REITZ, R.D. 1993 Mechanisms of air-assisted liquid atomization. *Atomiz. Spray* **3**, 55–75.

LIU, Z. & REITZ, R.D. 1997 An analysis of the distortion and breakup mechanisms of high speed liquid drops. *Intl J. Multiphase Flow* **23**, 631–650.

LU, J. & TRYGGVASON, G. 2018 Direct numerical simulations of multifluid flows in a vertical channel undergoing topology changes. *Phys. Rev. Fluids* **3** (8), 084401.

MAGNAUDET, J. & MOUGIN, G. 2007 Wake instability of a fixed spheroidal bubble. *J. Fluid Mech.* **572**, 311–337.

MARCOTTE, F. & ZALESKI, S. 2019 Density contrast matters for drop fragmentation thresholds at low Ohnesorge number. *Phys. Rev. Fluids* **4**, 103604.

MAXEY, M.R. & RILEY, J.J. 1983 Equation of motion for a small rigid sphere in a nonuniform flow. *Phys. Fluids* **26**, 883–889.

MEI, R., LAWRENCE, C.J. & ADRIAN, R.J. 1991 Unsteady drag on a sphere at finite Reynolds number with small fluctuations in the free-stream velocity. *J. Fluid Mech.* **233**, 613–631.

MENG, J.C. & COLONIUS, T. 2018 Numerical simulation of the aerobreakup of a water droplet. *J. Fluid Mech.* **835**, 1108–1135.

MIKAELIAN, K.O. 1990 Rayleigh–Taylor and Richtmyer–Meshkov instabilities in multilayer fluids with surface tension. *Phys. Rev.* A **42**, 7211.

MIKAELIAN, K.O. 1996 Rayleigh–Taylor instability in finite-thickness fluids with viscosity and surface tension. *Phys. Rev.* E **54**, 3676.

MIKSIS, M., VANDEN-BROECK, J.-M. & KELLER, J.B. 1981 Axisymmetric bubble or drop in a uniform flow. *J. Fluid Mech.* **108**, 89–100.

MOSTERT, W., POPINET, S. & DEIKE, L. 2022 High-resolution direct simulation of deep water breaking waves: transition to turbulence, bubbles and droplets production. *J. Fluid Mech.* **942**, A27.

NEEL, B., LHUISSIER, H. & VILLERMAUX, E. 2020 'Fines' from the collision of liquid rims. *J. Fluid Mech.* **893**, A16.

OPFER, L., ROISMAN, I.V., VENZMER, J., KLOSTERMANN, M. & TROPEA, C. 2014 Droplet–air collision dynamics: evolution of the film thickness. *Phys. Rev.* E **89**, 013023.

O'ROURKE, P.J. & AMSDEN, A.A. 1987 The TAB method for numerical calculation of spray droplet breakup. *Tech. Rep.* LA-UR-2105. Los Alamos National Laboratory.

PAI, M.G. & SUBRAMANIAM, S. 2006 Modeling interphase turbulent kinetic energy transfer in Lagrangian–Eulerian spray computations. *Atomiz. Spray* **16**, 807–826.

PARK, J.-H., YOON, Y. & HWANG, S.-S. 2002 Improved TAB model for prediction of spray droplet deformation and breakup. *Atomiz. Spray* **12**, 387–401.

PILCH, M. & ERDMAN, C.A. 1987 Use of breakup time data and velocity history data to predict the maximum size of stable fragments for acceleration-induced breakup of a liquid drop. *Intl J. Multiphase Flow* **13**, 741–757.

POPINET, S. 2009 An accurate adaptive solver for surface-tension-driven interfacial flows. *J. Comput. Phys.* **228** (16), 5838–5866.

RANGER, A.A. & NICHOLLS, J.A. 1969 Aerodynamic shattering of liquid drops. *AIAA J.* **7**, 285–290.

REYSSAT, E., CHEVY, F., BIANCE, A.-L., PETITJEAN, L. & QUERE, D. 2007 Shape and instability of free-falling liquid globules. *Europhys. Lett.* **80**, 34005.

RIMBERT, N., ESCOBAR, S.C., MEIGNEN, R., HADJ-ACHOUR, M. & GRADECK, M. 2020 Spheroidal droplet deformation, oscillation and breakup in uniform outer flow. *J. Fluid Mech.* **904**, A15.

SAKAKEENY, J., DESHPANDE, C., DEB, S., ALVARADO, J.L. & LING, Y. 2021 A model to predict the oscillation frequency for drops pinned on a vertical planar surface. *J. Fluid Mech.* **928**, A28.

SAKAKEENY, J. & LING, Y. 2020 Natural oscillations of a sessile drop on flat surfaces with mobile contact lines. *Phys. Rev. Fluids* **5**, 123604.

SAKAKEENY, J. & LING, Y. 2021 Numerical study of natural oscillations of supported drops with free and pinned contact lines. *Phys. Fluids* **33**, 062109.

SCARDOVELLI, R. & ZALESKI, S. 1999 Direct numerical simulation of free-surface and interfacial flow. *Annu. Rev. Fluid Mech.* **31**, 567–603.

SHARMA, S., SINGH, A.P., RAO, S.S., KUMAR, A. & BASU, S. 2021 Shock induced aerobreakup of a droplet. *J. Fluid Mech.* **929**, A27.

STEFANITSIS, D., MALGARINOS, I., STROTOS, G., NIKOLOPOULOS, N., KAKARAS, E. & GAVAISES, M. 2017 Numerical investigation of the aerodynamic breakup of diesel and heavy fuel oil droplets. *Intl J. Heat Fluid Flow* **68**, 203–215.

STEFANITSIS, D., MALGARINOS, I., STROTOS, G., NIKOLOPOULOS, N., KAKARAS, E. & GAVAISES, M. 2019*a* Numerical investigation of the aerodynamic breakup of droplets in tandem. *Intl J. Multiphase Flow* **113**, 289–303.

STEFANITSIS, D., STROTOS, G., NIKOLOPOULOS, N., KAKARAS, E. & GAVAISES, M. 2019*b* Improved droplet breakup models for spray applications. *Intl J. Heat Fluid Flow* **76**, 274–286.

STROTOS, G., MALGARINOS, I., NIKOLOPOULOS, N. & GAVAISES, M. 2016 Predicting droplet deformation and breakup for moderate Weber numbers. *Intl J. Multiphase Flow* **85**, 96–109.

TANG, K., ADCOCK, T. & MOSTERT, W. 2023 Bag film breakup of droplets in uniform airflows. *J. Fluid Mech.* **970**, A9.

TANNER, F.X. 1997 Liquid jet atomization and droplet breakup modeling of non-evaporating diesel fuel sprays. *SAE Trans. J. Engines* **106**, 127–140.

TAYLOR, G.I. 1949 The shape and acceleration of a drop in a high-speed air stream. In *The Scientific Papers of G.I. Taylor. Vol. III. Aerodynamics and the Mechanics of Projectiles and Explosions* (ed. G.K. Batchelor). Cambridge University Press.

THEOFANOUS, T.G. 2011 Aerobreakup of Newtonian and viscoelastic liquids. *Annu. Rev. Fluid Mech.* **43**, 661–690.

THEOFANOUS, T.G. & LI, G.J. 2008 On the physics of aerobreakup. *Phys. Fluids* **20**, 052103.

THEOFANOUS, T.G., LI, G.J. & DINH, T.-N. 2004 Aerobreakup in rarefied supersonic gas flows. *Trans. ASME J. Fluid Engng* **126**, 516–527.

THEOFANOUS, T.G., LI, G.J., DINH, T.-N. & CHANG, C.-H. 2007 Aerobreakup in disturbed subsonic and supersonic flow fields. *J. Fluid Mech.* **593**, 131–170.

THEOFANOUS, T.G., MITKIN, V.V. & NG, C.L. 2013 The physics of aerobreakup. III. Viscoelastic liquids. *Phys. Fluids* **25**, 032101.

THEOFANOUS, T.G., MITKIN, V.V., NG, C.L., CHANG, C.H., DENG, X. & SUSHCHIKH, S. 2012 The physics of aerobreakup. II. Viscous liquids. *Phys. Fluids* **24**, 022104.

TIWARI, S.S., PAL, E., BALE, S., MINOCHA, N., PATWARDHAN, A.W., NANDAKUMAR, K. & JOSHI, J.B. 2020*a* Flow past a single stationary sphere, 1. Experimental and numerical techniques. *Powder Technol.* **365**, 115–148.

TIWARI, S.S., PAL, E., BALE, S., MINOCHA, N., PATWARDHAN, A.W., NANDAKUMAR, K. & JOSHI, J.B. 2020*b* Flow past a single stationary sphere, 2. Regime mapping and effect of external disturbances. *Powder Technol.* **365**, 215–243.

VANDEN-BROECK, J.-M. & KELLER, J.B. 1980 Deformation of a bubble or drop in a uniform flow. *J. Fluid Mech.* **101**, 673–686.

VILLERMAUX, E. & BOSSA, B. 2009 Single-drop fragmentation determines size distribution of raindrops. *Nat. Phys.* **5**, 697–702.

VILLERMAUX, E. & BOSSA, B. 2011 Drop fragmentation on impact. *J. Fluid Mech.* **668**, 412.

WERT, K.L. 1995 A rationally-based correlation of mean fragment size for drop secondary breakup. *Intl J. Multiphase Flow* **21**, 1063–1071.

WILLIAMS, M.B. & DAVIS, S.H. 1982 Nonlinear theory of film rupture. *J. Colloid Interface Sci.* **90** (1), 220–228.

YANG, W., JIA, M., SUN, K. & WANG, T. 2016 Influence of density ratio on the secondary atomization of liquid droplets under highly unstable conditions. *Fuel* **174**, 25–35.

ZHANG, B., POPINET, S. & LING, Y. 2020 Modeling and detailed numerical simulation of the primary breakup of a gasoline surrogate jet under non-evaporative operating conditions. *Intl J. Multiphase Flow* **130**, 103362.

ZHAO, H., LIU, H.-F., XU, J.-L., LI, W.-F. & LIN, K.-F. 2013 Temporal properties of secondary drop breakup in the bag-stamen breakup regime. *Phys. Fluids* **25**, 054102.